

A New Liquid Metal-Air Battery

A Major Qualifying Project Report

submitted to

the Faculty of the WORCESTER POLYTECHNIC INSTITUTE

Chemical Engineering Department

in partial fulfillment of the requirements

for the Degree of Bachelor of Science

by

Tyler Trettel Howard

Stephen Patrick Johnston

Laura Christine Merrill

Date: April 30, 2015

Adviser: Ravindra Datta

This report represents the work of WPI undergraduate students submitted to the faculty as evidence of completion of a degree requirement. WPI routinely publishes these reports on its website without editorial or peer review. For more information about the projects program at WPI, please see <http://www.wpi.edu/academics/ugradstudies/project-learning.html>

Abstract

Increasing demand for renewable energy requires a shift to microgrids with energy storage systems. Liquid metal-air flow batteries have theoretically high energy densities and long life cycles, satisfying microgrid requirements. A proof of concept for this battery was established with a gallium-air electrochemical cell to determine performance and limiting factors. It was determined that the gallium-air chemistry was feasible, achieving a flat discharge profile for over 4.7 hours on average. Electrolyte carbonation, separator drying, and oxide layer formation hindered performance.

Table of Contents

Abstract	2
Introduction	8
1.1 Energy Storage Issues	8
1.2 Overview of Batteries	10
1.3 Project Vision	11
1.4 Summary of Work Accomplished	13
2 Literature Review	14
2.1 Secondary Battery Chemistry	14
2.2 Flow Batteries	16
2.3 Conventional Primary Metal-Air Batteries	18
2.3.1 Rechargeable Metal-Air Flow Batteries	21
2.4 Liquid Metal Batteries	23
2.5 Liquid Metal-Air Batteries	25
2.5.1 Liquid Gallium Anode Potential	26
2.6 Electrochemical Reactions for Liquid Metal-Air Batteries	27
2.6.1 Oxygen Reduction and Evolution Reaction	28
2.6.2 Liquid Metal Electrode Oxidation and Reduction in Alkaline Media	29
3 Methodology	32
3.1 Design of the Battery	32
3.2 Materials	32
3.2.1 Mechanical Parts	32
3.2.2 Liquid Metal Anode	33
3.2.3 Electrolyte and Separator	34
3.2.4 Air Cathode	34
3.3 Electrochemical Cell Set Up and Testing	34
3.3.1 Zirconia Cloth Electrolyte Fabrication	36
3.3.2 Anion Exchange Membrane Procedure	36
3.3.3 Pure Oxygen Testing	37
3.4 Battery Analyzer Testing Procedure (BAWIN500 Program)	37
3.4.1 Polarization Testing	37
3.4.2 Discharge Testing	38

4 Results	39
4.1 Theoretical Calculations	39
4.1.1 Open Circuit Voltage.....	39
4.1.2 Electrochemical Equivalent, Capacity and Service Life	41
4.1.3 Gravimetric and Volumetric Energy Density	42
4.2 Open Circuit Voltage (OCV) Results	43
4.2.1 Average OCV Testing Results	43
4.2.2 Experimental OCV Comparison to Theoretical.....	45
4.3 Polarization Testing	46
4.3.1 Polarization Plots	46
4.3.2 Tafel Plots	50
4.3.3 Polarization Modeling.	52
4.4 Discharge Performance: Establishing a Baseline	55
4.5 Discharge Performance: Effect of Variables.....	61
5 Conclusions and Recommendations	69
References	72
APPENDIX	79
Appendix A: Anode Procedure and General Cell Assembly	79
Appendix B: Electrolyte Procedure.....	79
B.1 Zirconia Paper	79
B.2 Anion Exchange Membrane.....	80
Appendix C: Cathode Procedure.....	81
Appendix D: Swagelok Assembly Procedure.....	81
Appendix E: Battery Analyzer Program (BA500WIN) User Guide	85

Table of Figures

Figure 1: Electrical energy storage technologies for grid applications (Dunn et al., 2011).....	9
Figure 2: General electrochemical cell (Kiehne, 2003)	11
Figure 3: Generic depiction of liquid gallium-air flow battery	12
Figure 4: Flow of electrons for discharge (left) and charge (right) (Rahman et al., 2013).....	14
Figure 5: Lithium ion transfer between charging and discharging (Horiba, 2014)	16
Figure 6: Flow battery schematic (Skyllas-Kazacos et al., 2011)	17
Figure 7: Zinc-bromine hybrid flow battery general schematic (Skyllas-Kazacos, et al., 2011)..	18
Figure 8: Commercial primary Zn-air battery (size D13) cutout showing:	19
Figure 9: Zn-air cell assembly with two air cathodes (Deiss, et al., 2002)	20
Figure 10: Refuelable Zn-air battery energy storage system (Pei et al., 2014).	22
Figure 11: Electrochemically rechargeable Zn-air flow battery design (Amendola et al., 2012).	23
Figure 12: Liquid metal battery schematic during a) discharging b) charging (Kim et al., 2012)	23
Figure 13: Orange elements are negative electrode candidates. Green elements are positive electrode candidates.	24
Figure 14: General high temperature liquid metal air battery schematic showing redox reactions during charging and discharging cycles (Otaegui et al., 2014).	27
Figure 15: Schematic of oxygen reduction at porous gas diffusion membrane (Cheng and Chen, 2012)	28
Figure 16: Pourbaix diagram for gallium. Dashed line represents thermodynamically stable region (Schweitzer, 2009).	30
Figure 17: Exploded view (left) and collapsed view (right) of the Swagelok Ga-air cell design .	32
Figure 18: Stainless steel electrode current collector mechanical drawings. Anode (top), cathode (bottom).	33
Figure 19: Heating instruments tested with their respective temperature profiles.	35
Figure 20: Ring stand and heating lamp set up with cell orientation shown.	36
Figure 21: OCV vs Temperature	44
Figure 22: Polarization performance of Ga-air cell with zirconia cloth wetted with aqueous 33.6 wt.% KOH electrolyte at 40 °C. Theoretical OCV for Ga ₂ O ₃ (solid black line) = 1.724 V. Theoretical OCV for Ga(OH) ₃ (broken black line) = 1.643 V.	46

Figure 23: Polarization comparison for Ga-air cells with wetted zirconia cloth at 40 °C and 75 °C.	48
Figure 24: Polarization comparison for Ga-air cells with wetted zirconia cloth and anion exchange membrane (AEM) assemblies at 50 °C.	49
Figure 25: Polarization curves for a commercial Zn-Air cell, a Ga-Air cell with a zirconia separator, and a Ga-Air cell with an AEM.	50
Figure 26: Tafel plots for Ga-air cell with 33.6 wt.% KOH wetted zirconia cloth at 65°C. Overpotential shown for gallium oxide (a) and gallium hydroxide (b).	51
Figure 27: Tafel plots for Ga-air cell with 33.6 wt.% KOH wetted anion exchange membrane at 65°C. Overpotential shown for gallium oxide (a) and gallium hydroxide (b)	52
Figure 28: Correlation constants relating conductivity of KOH by weight percent and temperature.	54
Figure 29: a) Model for Ga-air cell with zirconia cloth compared to experimental data. b) Model for Ga-air cell with an AEM compared to experimental data.	55
Figure 30: Image of a short circuited cell attributed to gallium leakage	57
Figure 31: Ga-air cell discharge curve at 40°C	58
Figure 32: Zn-air button cell discharge at room temperature	58
Figure 33: Ga-air cell potential vs capacity	59
Figure 34: Zn-air cell potential vs capacity discharge curve	60
Figure 35: 12.6 hour discharge time with zirconia cloth separator	61
Figure 36: The effects of cell agitation on zirconia cloth discharge performance	62
Figure 37: The addition of PTFE to zirconia cloth separator	63
Figure 38: Each discharge test for zirconia cloth at various temperatures	64
Figure 39: Discharge curve of zirconia cloth at 88°C in an oven	65
Figure 40: Discharge with zirconia cloth separator with a pure O ₂ feed at approximately 40°C.	66
Figure 41: Discharge results of Figure 22 upon re-wetting after termination with a pure O ₂ feed at approximately 40°C	67
Figure 42: Discharge test results of AEM separator	68
Figure 43: Heating gallium in glass vial under a heating lamp (left). Soaking zirconia cloth separator in 30 wt.% KOH (right).....	81

Figure 44: Ferrule orientation on anode current collector (left) in Swagelok PTFE fitting (right).
.....82

Figure 45: Swagelok PTFE union connected to fitting holding anode current collector (left).
Addition of compression spring (right).....82

Figure 46: Addition of stainless steel crucible to top of compression spring (left). Addition of
liquid gallium to the crucible using a syringe (right).....82

Figure 47: View of liquid gallium in crucible (left). Teflon gasket above anode crucible (right).
.....83

Figure 48: Zirconia cloth separator wetted with 30 wt.% KOH above the gasket (left). Catalyzed
gas diffusion layer above separator, with platinum coated catalyst facing the electrolyte (right).83

Figure 49: Ferrule orientation on air cathode current collector (left) with Swagelok fitting added
(right).....83

Figure 50: Completed cell configuration (left. Cell held by a ring stand clamp under a heating
lamp oriented so that liquid metal anode is above the air cathode (right).....84

Figure 51: Taped temperature probe from battery analyzer taped to the Swagelok fitting on the
air cathode side of the cell (left). Analyzer cathode and anode electrical leads attached to current
collector (right).84

Figure 52: Start page of the BA500WIN program. Features a real time graph that charts voltage,
current and temperature.....85

Figure 53: Programs drop down menu opened. Tests can be made with the program editor.85

Figure 54: By choosing edit program from the programs dropdown menu, the program editor
window opens.86

Figure 55: The second tab of the program editor requires a step function. To gather an open
circuit voltage measurement, the pause function can be chosen.87

Figure 56: The third tab of the program editor lets the user define the parameters of the test.87

Figure 57: Often it is necessary to change the analyzer options which can be found from the drop
down menu shown above or by keyboard shortcut F2.....88

Figure 58: The analyzer options window opens when prompted to show various tabs ranging
from ‘general’ to ‘environment.’88

1 Introduction

1.1 Energy Storage Issues

Undeniably, the consumption of energy is projected to grow in years moving forward with increased global population and industrialization. World consumption of energy is projected to increase by 37% by 2040 according to the International Energy Agency (IAE, World Energy Outlook 2014, 2014). To meet the current demand, most energy is generated from fossil fuels. The projected growth in energy consumption poses inherent environmental issues associated with greenhouse gas emissions from fossil fuel combustion. Power generated by fossil fuels has been linked to 40% of carbon dioxide emissions that affect global climate change (Bouhafs et al., 2014). Additionally, fossil fuels are not sustainable and pose a national security risk with foreign dependence. Thus, governments have been pushing to integrate cleaner sources of energy such as renewables. Moving forward, renewables are projected to comprise one-third of the global generation market by 2040. Already, renewable power capacity expanded at its fastest pace to date accounting for 22% of global power generation in 2013 (IAE, Mid-term Market Report, 2014). This trend is expected to continue with wind and solar power becoming more pervasive.

Increasing demand for renewable energy resources has brought attention to the need for a more reliable and resilient electrical grid with energy storage systems. Wind and solar power are intermittent energy sources that produce variable amounts of electricity through the day, depending on the amount of wind or sunlight available. The variability can significantly affect the electrical grid's operation (Sarasua et al., 2013). Today's grid infrastructure supplies power the instant it is produced to meet a demand. Wind and solar variability is an issue because the time of power generation does not match the consumption demand. Grid operators additionally cannot determine where and how much power is being generated at any given moment, adding complexity to the issue. To integrate renewable energy to the grid efficiently, a smarter grid is needed.

One solution to the aging grid infrastructure is to use smaller decentralized energy generation and distribution systems, referred to as a microgrids. A microgrid is a smaller power grid specific to a certain area with capability for efficient onsite control of energy consumption and production (Bouhafs et al., 2014). This system can be connected or isolated from the grid to

enhance local reliability. Microgrids offer a solution to modernizing the grid for renewable integration by incorporating on-site energy storage technologies.

The variable nature of renewables can be balanced by energy storage. A reliable energy storage system functions as an energy backup to improve power quality by counteracting the imbalance between instantaneous supply and demand that varies throughout the day. Thus, the power generated by wind and solar power can be stored when not in demand and supplied when needed. Potential energy storage systems for microgrid applications are commonly represented by batteries, super-capacitors, and flywheels (Hu and Liaw, 2013). Applications for various energy storage technologies are shown in Figure 1 (Dunn et al., 2011).

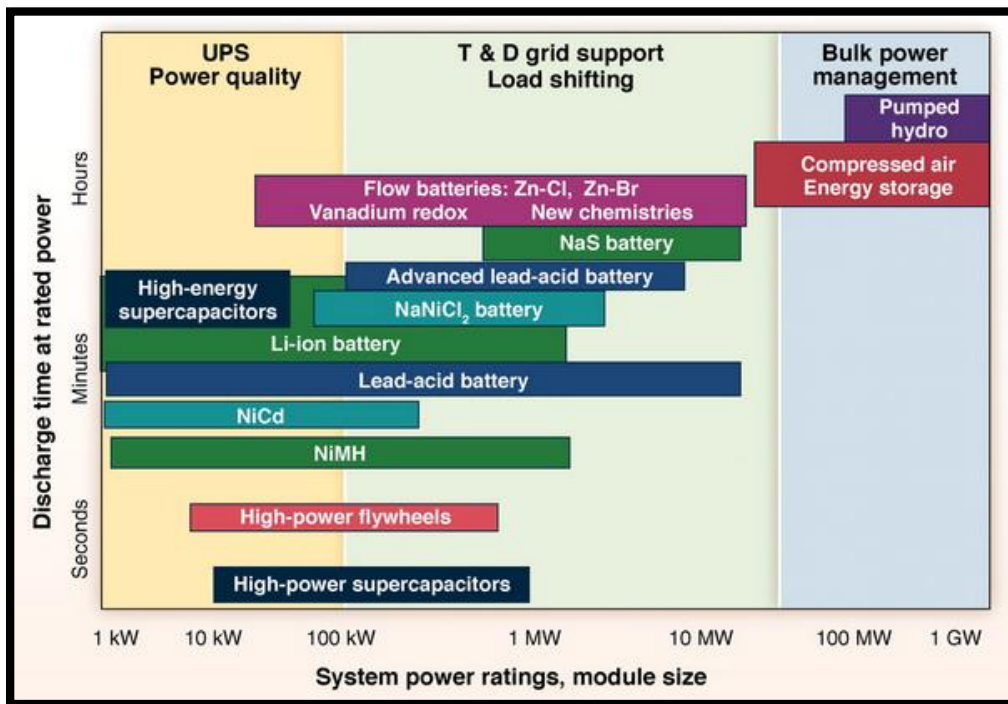


Figure 1: Electrical energy storage technologies for grid applications (Dunn et al., 2011)

For transmission and distribution grid support load shifting due to renewable integration, batteries are best suited because of their modular scalability and discharge time. Batteries are the leading energy storage technology to provide both high power and energy densities for extended periods (Fu et. al, 2013). Lead acid batteries are the current dominating battery energy storage technology due to their proven performance and low cost (Castillo and Gayme, 2014). However,

these batteries can only discharge at their rated power in minutes when hours are more suitable for grid applications. They are also composed of toxic materials, have low energy density and limited cycle life, requiring large battery banks with frequent maintenance. Lithium based batteries are another possible energy storage candidate. These batteries also face energy density issues and limited life cycle to a lesser extent than lead acid but cost more. Flow batteries are promising because they are theoretically capable of long life cycles. Although still hindered by energy density limitations, the power and energy components can be separated and scaled up. Metal-air battery research has gained ground recently due to its high theoretical energy density as a result of one electrode being an unlimited and free atmospheric air supply. The most developed metal-air battery utilizes zinc-air chemistry and is commercialized as a primary battery for small portable applications. Problems with rechargeable performance and lifecycles currently hinder this technology for grid applications (Berecibar & Zhou, 2013). These issues have been linked to the formation of dendrites on the zinc metal electrode and carbonation of the alkaline potassium hydroxide electrolyte (Lee et al., 2011). Today's battery energy storage technology is not yet suitable for grid applications. There is a clear need for a low cost rechargeable battery with high energy density and long life cycle capability.

1.2 Overview of Batteries

Batteries are electrochemical energy storage devices that store electrical energy as chemical energy. They can be divided up into two categories: primary (single use) and secondary (rechargeable). An example of a primary battery is the alkaline batteries that are used to power common household objects such as clocks or remote controls. Examples of secondary batteries include nickel metal hydride and lithium ion batteries, commonly used in many electronic devices such as laptops or cellphones.

The electrochemical cell that makes a battery operate consists of two electrodes and an electrolyte. It is the material of the two electrodes and electrolyte that define the overall chemical reactions. Batteries work by utilizing oxidation and reduction, or redox, reactions to convert chemical potential energy to electricity. These redox reactions result in the exchange of electrons from the electrodes to create a flowing electric current to an external load. During discharge, one electrode becomes positive (cathode) as it is reduced into its ions. These ions are transported through an electrolyte to the other electrode, making it negative (anode). The opposite process

takes place during charging. Suitable electrolytes are usually liquid solutions of acids, alkalis, or salts. The capacity of the battery may be increased by increasing the number of cells. Figure 2 shows the setup of an electrochemical cell and the generic reactions that take place.

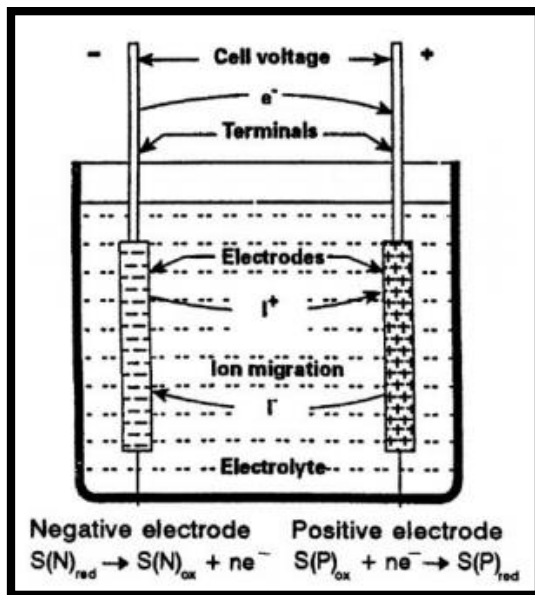


Figure 2: General electrochemical cell (Kiehne, 2003)

1.3 Project Vision

Battery energy storage technology is critical to further integrate renewable energy to the electrical grid. The intention of this investigation is to contribute to the development of battery energy storage for renewable power generation applications. Since wind and solar power technologies are naturally intermittent; the use of a battery for electrochemical energy storage can help even out power generation to better meet the demands of the grid.

This investigation's vision specifically focuses on the development of a liquid metal-air flow battery. Flow batteries are promising candidates for renewable energy applications because of their theoretically long life cycles, but lack the necessary energy density needed at the grid scale. Metal-air batteries have high theoretical energy density with extended discharge service life, but are primarily non-rechargeable. This battery's cathode uses a freely abundant air supply with less space, weight, and cost compared to a typical cathode material. However, the air cathode undergoes sluggish kinetics and needs to be bi-functional for rechargeability. Combining the advantageous aspects and addressing the issues of both flow and metal-air batteries would theoretically yield an ideal battery for renewable energy storage.

A proposed liquid metal-air flow battery that consists of a liquid gallium anode, aqueous alkaline electrolyte and air cathode (Figure 3) is a potential solution. Metal-air batteries are non-rechargeable in part due to the anode material (typically zinc) undergoing shape change and dendrite formation during the charging process. A circulating liquid metal anode material alleviates these issues. Gallium is a good candidate material because it is non-toxic, has a low melting point, and has good electrochemical properties. The alkaline electrolyte will be circulated in a similar manner to eliminate any losses due to carbonation or evaporation.

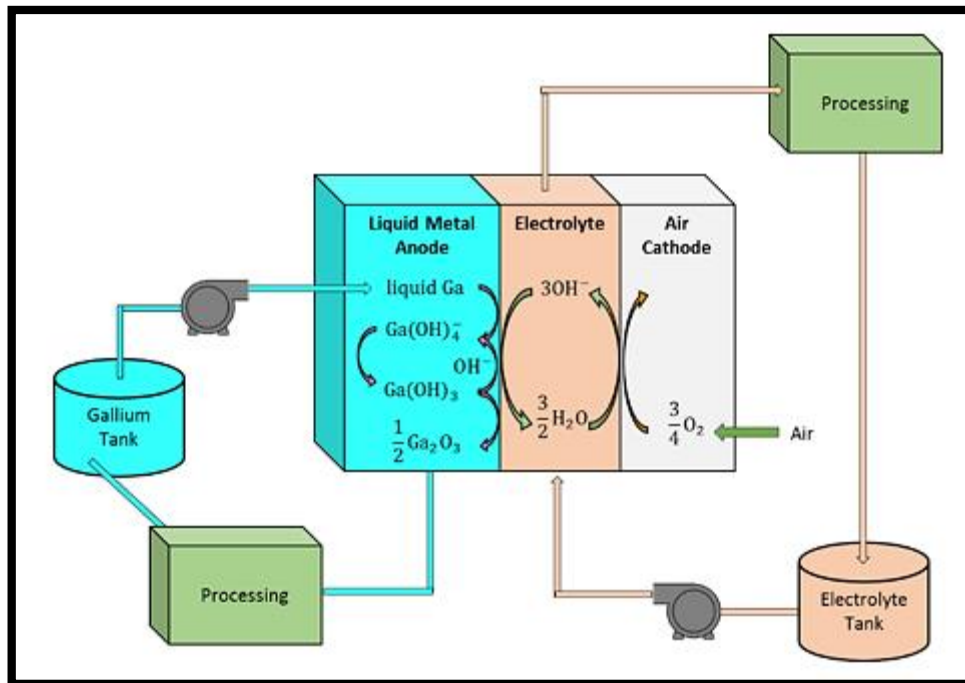


Figure 3: Generic depiction of liquid gallium-air flow battery

The development of a liquid metal-air flow battery acted as an overarching goal for this investigation. A prototype Swagelok cell design was used to first explore the feasibility of the gallium-air cell's electrochemical reactions and their performance limitations. This prototype differs from the flow battery design by incorporating horizontally layered and static internal components. Research was conducted on the cell to achieve the following project goals:

- Validate the proof of concept of a gallium-air cell by obtaining an open circuit voltage competitive to existing technologies

- Establish a reproducible polarization and discharge performance baseline and identify limiting factors
- Mathematically model the polarization performance and compare to experimentally obtained data
- Determine methods to address performance limitations for scaled up flow battery design

1.4 Summary of Work Accomplished

This report is a summation of the work accomplished in effort towards developing a new liquid gallium-air flow battery. Literature review was conducted for a variety of topics including general secondary battery electrochemistry, relevant battery energy storage technologies, and a review of the thermodynamically favorable redox reactions of a gallium-air cell. The methodology outlines the procedures used to create and test a prototype Swagelok cell design. The prototype was tested and compared to theoretically calculated values in the results section.

Research goals were met throughout this investigation. The feasibility of the gallium-air cell was validated by obtaining open circuit voltages ranging from 1.1-1.4 V. This is comparable to commercial zinc-air batteries that obtain potentials of 1.4 V and fuel cells that are typically less than 1 V. Moreover, polarization and discharge performance at several temperatures were reproduced and compared to theoretically obtained values and existing zinc-air technology. A working theoretical model matched the experimental polarization curves obtained. The prototype had a desirable flat discharge profile at a constant current drain consistently over 10 hours at ambient temperatures ranging from 50-60 °C. However, the capacity was considerably less than its theoretical capability as well as in comparison to zinc-air. Factors such as electrolyte evaporation and carbonation were identified as possible performance limitations. Despite the problems, the results are promising and can be alleviated with a flow battery design. New battery development is a long term process and the work provided here sets the initial stage for further advancement.

2 Literature Review

This chapter provides a brief review of literature relevant to liquid gallium-air flow battery technology. General secondary battery electrochemistry is explored to understand the fundamental principles of operation. Following is a review of several battery energy storage technologies including flow batteries, all liquid metal batteries, as well as primary and secondary metal-air batteries. In closing, the electrochemistry specific to liquid gallium-air redox reactions in aqueous alkaline media is investigated.

2.1 Secondary Battery Chemistry

As with traditional primary batteries, a secondary battery is made up of two electrodes and an electrolyte layer. However, unlike traditional batteries – where one electrode is negative, the anode, and one is positive, the cathode – the charge of the electrodes is reversed during the charging process (Kiehne, 2003). During discharge, the negative electrode material is oxidized and the positive electrode is reduced, allowing for the flow of electrons. The reactions and electron flow are reversed while the cell charges, which reverses the charge of the electrodes. Figure 4 shows the change in flow of electrons between discharge (left) and charge (right) for the zinc-air battery.

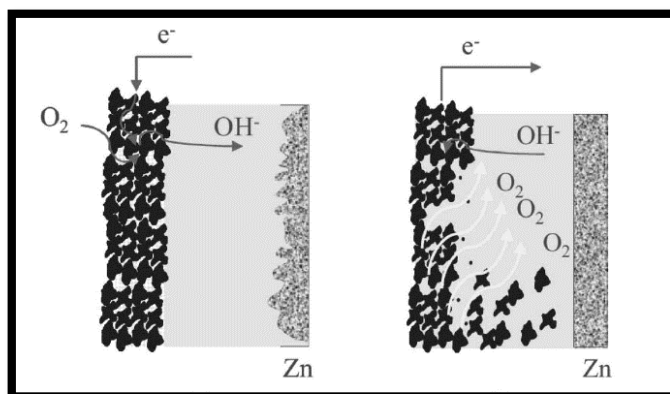


Figure 4: Flow of electrons for discharge (left) and charge (right) (Rahman et al., 2013)

The performance of a battery is dependent on the thermodynamics and kinetics of the reactions (Cheng et al., 2011). It is the thermodynamics of the reaction that determines the theoretical voltage, reversibility and energy densities of batteries. The practical values observed are often

much lower than the calculated theoretical values. According to Cheng, et al. (2011), “the major reasons for this limitation include slow electrode process kinetics with high polarization and a low rate of diffusion or electronic conductivity, particularly at the electrode interfaces.” These losses are primarily related to the overpotential associated with activation losses and mass transfer limitations. To improve upon the efficiency of secondary batteries, many researchers have focused on molecular and ionic transport, cell structure, the electrochemical reactions, and the materials in use.

To improve upon secondary battery technology, there is a focus on minimizing cost while maximizing capacity, reversibility, and electron transfer. The engineering design of the battery can also have a strong impact on its success. For instance, because the reactions occur at the surfaces of the electrodes, a high surface area can be favorable so there are more sites for ions to interact. A greater surface area can cost additional expenses to the cost of the cell. In addition, the separator must allow only the transfer of ions and not be electronically conductive, adding to the expense (Arnold, 2007). The formation of metal oxide at the surface interface may also hinder the transport that allows the redox reactions to continue. However, in the case of metal-air batteries, the oxide is one of the products of discharging based on the reactions to produce a current. Many of the batteries that are being developed have a trade-off between performance and price.

A great deal of research is going into the development of rechargeable batteries for various purposes including portable electronics, automotive, and grid storage. For automotive and portable electronics, the most popular battery in use is lithium-ion. These are attractive due to their high theoretical power density and slow discharging rate, making it the frontrunner of secondary batteries. Lithium-ion batteries “utilize(s) insertion reactions for both positive and negative electrodes with Li ions as charge carriers” (Horiba, 2014). During charging, lithium-ions transfer from the cathode to the anode, and for discharging the transfer is reversed. This process is shown in Figure 5, and some commonly used materials include porous graphite at one electrode and metal oxides at the other. The state of the lithium is reduced in the graphite electrodes and oxidized in the metal oxide electrode (i.e. redox reactions of lithium are involved). As previously mentioned, despite the success of lithium-ion batteries, they are not suitable for large scale energy storage applications due to inevitable loss of performance over

time and inadequate energy density. To apply these batteries for grid storage, battery banks will have to contain many batteries and would be very costly.

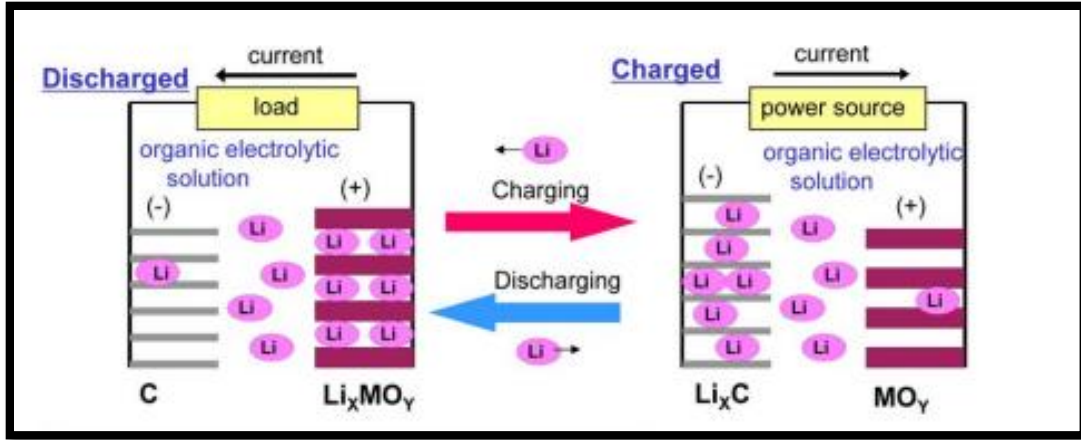


Figure 5: Lithium ion transfer between charging and discharging (Horiba, 2014)

2.2 Flow Batteries

Flow batteries are a type of secondary battery that employs redox states of different electrode materials immersed in liquid electrolytes for charging and discharging purposes. In some instances, they may be considered “electrochemically regenerative fuel cells” as they incorporate electrochemically rechargeable cell stacks with an external energy fuel source (Skylas-Kazacos et al., 2011). A flow battery’s power comes from cells connected in either parallel or series. The battery’s energy component comes from scalable tanks external to the cell stack filled with dilute aqueous electrolyte containing either anode or cathode material that is pumped to the cell stack. Within a cell, an ion-selective membrane separates the two solutions from mixing while allowing for adequate ion transfer to allow the redox reactions to occur. The electron transfer takes place at the electronically conductive porous electrodes of the cell. Figure 6 shows the general schematic of a flow battery.

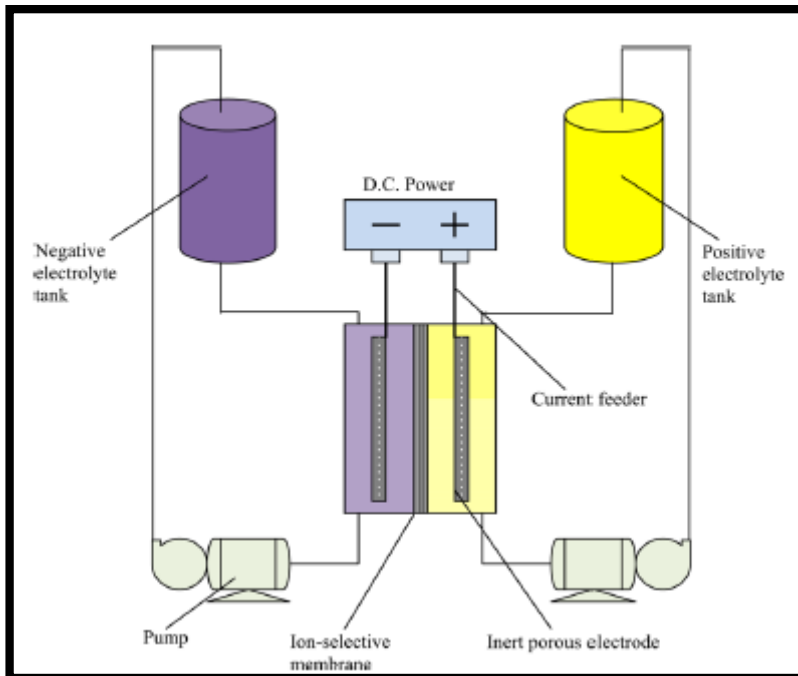


Figure 6: Flow battery schematic (Skylas-Kazacos et al., 2011)

Flow batteries are an attractive energy storage technology because of their theoretically long life cycle capability with efficiencies up to 85% (Skylas-Kazacos et al., 2011). The capacity of a flow battery may be varied depending on the size of the storage tanks used and number of cells stacked. Different electrical potentials result through use of different electrolytes. However, flow batteries have faced issues such as low energy densities, crossover of the electrolyte, and corrosion.

Hybrid flow batteries have been developed, including zinc-bromine batteries for example (Figure 7). These batteries are different from traditional flow batteries because one of the redox species is insoluble and may be present as either a metal or a gas (Skylas-Kazacos et al., 2011). Hybrid flow batteries have a similar efficiency to their traditional counterpart and also experience crossover issues. Unlike redox flow batteries, however, the energy storage capacity of a hybrid flow battery is dependent upon the structure and thickness of the metallic layer formed.

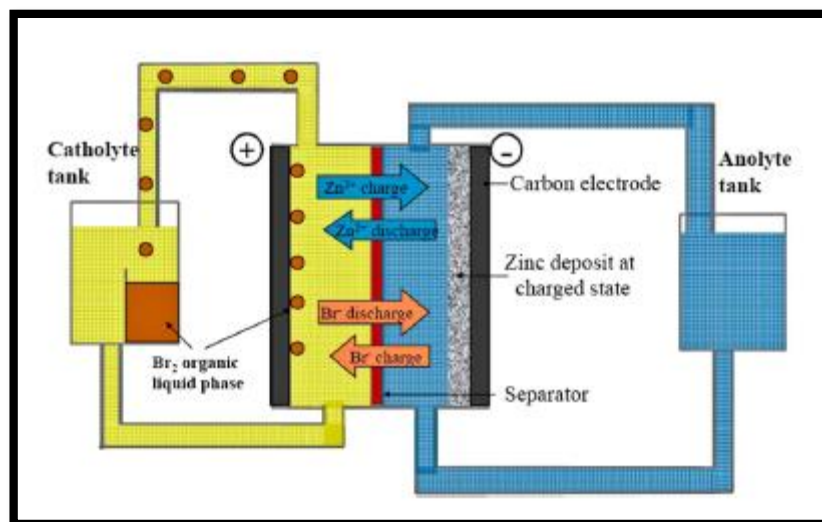


Figure 7: Zinc-bromine hybrid flow battery general schematic (Skylas-Kazacos, et al., 2011)

Despite the benefits of flow batteries, all of the presented batteries are ultimately limited by low energy densities. While it is possible to slightly change the energy density by changing the electrolyte concentrations, the reaction chemistry is the primary limiting factor. In order to achieve more favorable energy densities, different anode and cathode material may be used.

2.3 Conventional Primary Metal-Air Batteries

Metal-air batteries have recently attracted attention as an electrochemical energy storage device due to their high theoretical energy densities. The high energy density comes from an open cell structure which allows the batteries to use ambient air as the cathode, allowing the majority of the constructed cell to be comprised of just the anode and electrolyte. Attention has been given to Zn-air batteries as zinc is abundant, low cost, has low equilibrium potential, and has a flat discharge voltage (Lee et al., 2011). Additionally, zinc experiences less corrosion in alkaline solutions, as compared to other possible candidates such as aluminum. Zn-air batteries have been commercialized as primary button cells by several manufacturers including Duracell. These cells contain an alkaline electrolyte and zinc mixed with potassium hydroxide electrolyte solution (Figure 8). They come with the air cathode holes covered to prevent air from entering the cathode prior to use. This stops the carbonation and/or drying of the potassium hydroxide solution prior to use since both processes limit the performance of the battery. Moreover, by suspending the zinc in a type of three dimensional matrix with the electrolyte, the performance of

this battery has been optimized by drastically increasing the number of reaction sites on the cell anode.

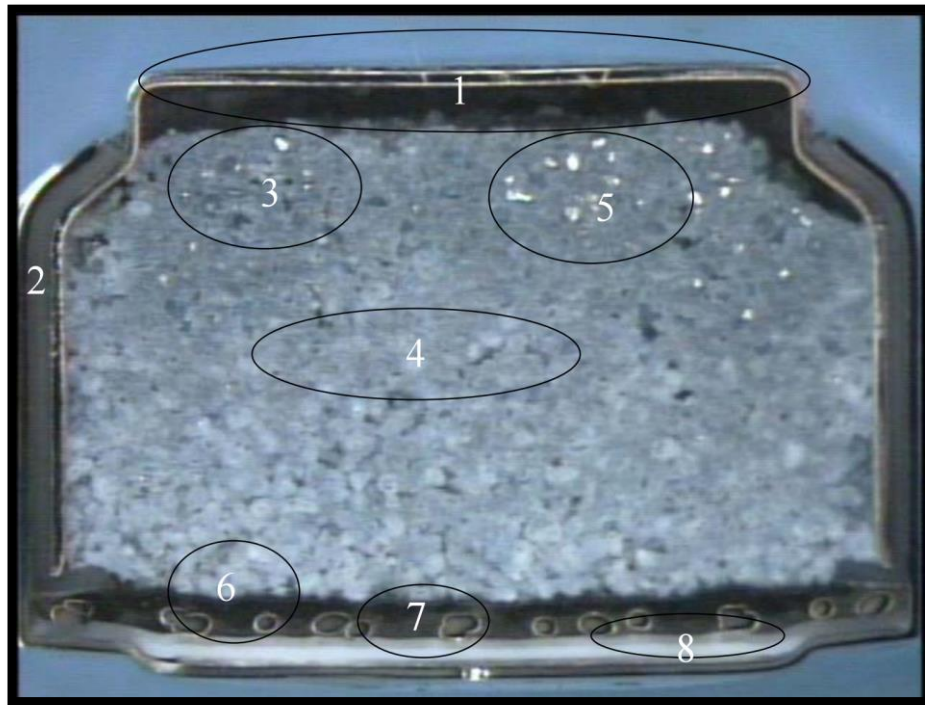


Figure 8: Commercial primary Zn-air battery (size D13) cutout showing:

- (1) Headspace in cell*
- (2) Electrical insulation to prevent short circuiting*
- (3) Type II discharged Zn particles*
- (4) Type I discharged Zn particles*
- (5) Non-discharged Zn particles*
- (6) Mesh screen for cathode assembly*
- (7) PTFE layer for cathode assembly*
- (8) MnO₁ catalyzed gas diffusion layer*

The secondary, or rechargeable, capabilities of Zn-air batteries have been limited, as shown through the cycling tests. Deiss et al. (2002) worked to numerically model a rechargeable, alkaline Zn-air cell in hopes that it could help to identify and alleviate challenges. This research group also performed experiments on a Zn-air battery that employs an air cathode on either side,

similar to a fuel cell design, and used pure oxygen as opposed to ambient air. This battery design is displayed in Figure 9.

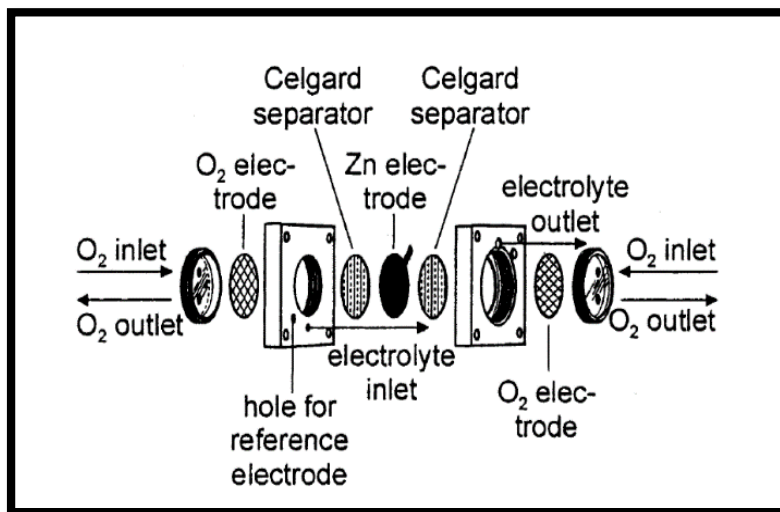


Figure 9: Zn-air cell assembly with two air cathodes (Deiss, et al., 2002)

Despite the advantages, liquid metal batteries are hindered by elevated operating temperatures ($> 200\text{ }^{\circ}\text{C}$), low theoretical specific energy densities ($< 200\text{ Wh kg}^{-1}$), low equilibrium cell voltages ($< 1.0\text{ V}$), corrosive materials and high discharge rates for some electrode pairs. The high operating temperature is costly and requires energy to be taken from another source and can lead to corrosion. The corrosiveness of the materials and operating temperatures factor into the low energy densities. Alloyed metals are an option to combat the issues that pure liquid metal batteries face. Through experimentation using charge cycles, they found that the morphological changes, including dendrite formation, within the anode and ion depletion had the greatest effect on the rechargeable performance of the battery. Additionally, the carbonation of an alkaline electrolyte was found to hinder its performance. In addition to these challenges, a special, bi-functional oxygen catalyst would be needed to allow the battery to charge.

Lithium-air batteries have also been explored as another metal-air battery option; however, they have not generated much success. Aside from its high reactivity, lithium experiences similar challenges to zinc regarding its rechargeable capabilities when a liquid electrolyte solution is used, including morphological changes. However, lithium-air batteries have experienced success

in cycling when a solid electrolyte interphase (SEI) forms on the anode (Lee et al., 2011). This helps to stabilize the lithium and suppress dendrite formation. However, these SEI layers can easily crack or break.

2.3.1 Rechargeable Metal-Air Flow Batteries

Metal-air flow batteries operate by the same principles of a typical flow battery by separating power (cell stack) and energy (electrolyte) components while addressing the issues of primary metal-air cells. The difference between primary metal air batteries and metal-air flow batteries is a circulating electrolyte. What differs from conventional flow batteries is the use of a circulating air supply at the cathode. The most developed metal-air flow battery technology for grid applications utilizes Zn-air chemistry with a suitable electrolyte system. These batteries are designed to be either mechanically or electrochemically rechargeable.

Mechanically rechargeable Zn-air flow batteries or fuel cells can be further categorized into reconstructable or refuelable cells (Xu et al., 2015). A reconstructable cell is designed to allow for the physical removal of spent zinc material usually in the form of a plate. Refuelable cells pump aqueous electrolyte containing zinc electroactive fuel. Zinc fuel can also be regenerated from its oxidized form by electrolysis. Pei et al. (2014) developed a refuelable Zn-air flow battery shown in Figure 10. A mechanical filling device feeds zinc pellets to the anode chamber of each cell while alkaline aqueous electrolyte (40 wt.% KOH) entrained with zinc particles is circulated.

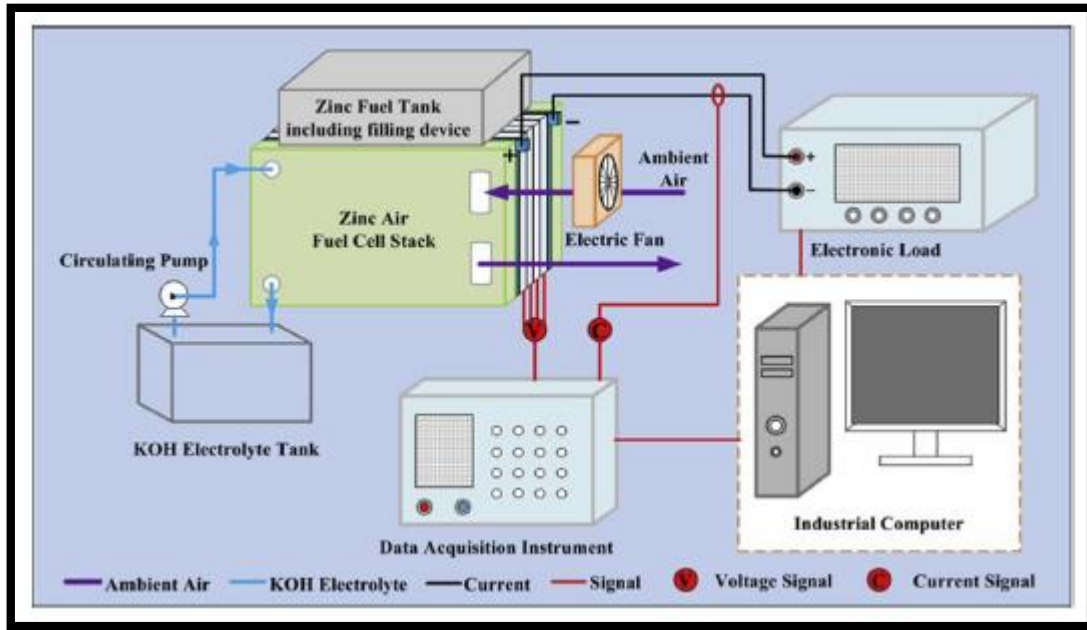


Figure 10: Refuelable Zn-air battery energy storage system (Pei et al., 2014).

Electrically rechargeable Zn-air flow batteries are promising for renewable integration. Solar or wind power can electrically recharge the cell and regenerate zinc fuel. This design requires less mechanical complexity but faces further challenges with dendrite formation and shape change. With a mechanically rechargeable Zn-air battery, this issue is avoided. Additionally, bi-functional air electrodes are needed that are susceptible to high overpotential, catalyst loss, and corrosion due to the oxygen evolution and reduction reactions.

Recent success has been developed by Amendola et al. (2012) by using a horizontal cell configuration shown in Figure 11. Notably, this design uses a third electrode for charging purposes to alleviate the issues faced with a bi-functional electrode. Deformation of the zinc anode and carbonation is avoided by using a slightly acidic electrolyte. Also, no separator material is needed because a horizontal design allows gravity to separate the cell components to avoid short-circuiting, simplifying the manufacturing process and significantly reducing price. Amendola joined EOS Energy Storage, a company which claims this design is capable of 10,000 cycles (30 calendar years) at a competitive $\$160 \text{ kWh}^{-1}$. Although not readily available until 2016, the technology claims to have solved the issues associated with rechargeable Zn-air batteries (Business Wire, 2015).

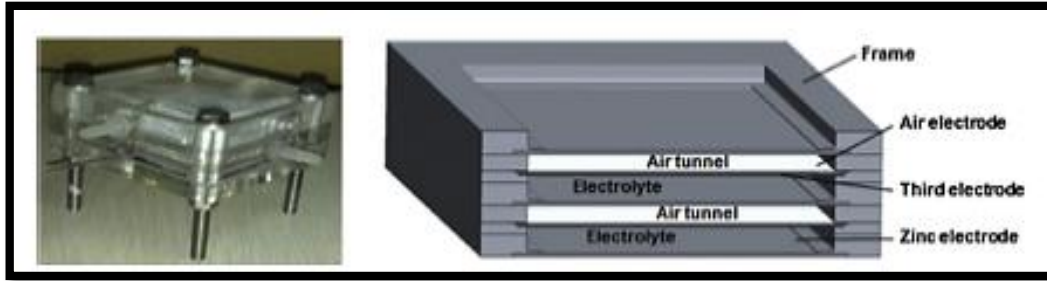


Figure 11: Electrochemically rechargeable Zn-air flow battery design (Amendola et al., 2012).

2.4 Liquid Metal Batteries

Liquid metal batteries are a relatively new type of secondary battery composed of a liquid metal anode and cathode separated by a molten salt electrolyte (Kim, 2012). Figure 12

Figure 12 depicts how the structure of the three layered cell works.

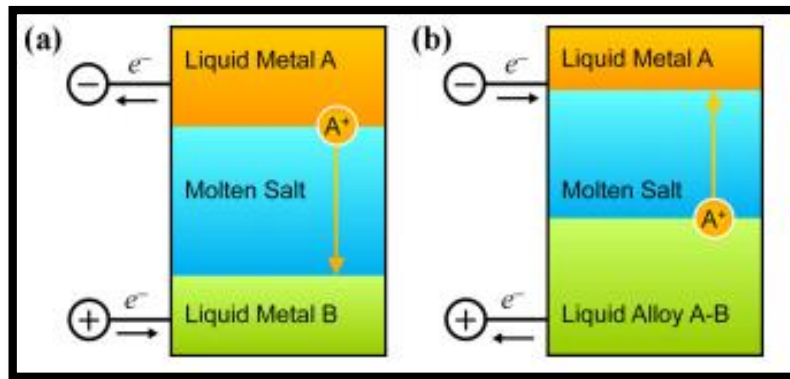


Figure 12: Liquid metal battery schematic during a) discharging b) charging (Kim et al., 2012)

The liquid metal electrodes and molten salt electrolyte are separated as shown due to their surface tension, immiscibility, and density differences. This self-aggregating structure of the cell allows for easy assembly. The complete cell is also self-sustaining with both discharging and charging cycles.

During a liquid metal battery's discharge cycle, the negative electrode metal is oxidized into ions, releasing electrons to flow external to the circuit towards the positive electrode (Sadoway, 2003). Simultaneously, cations from the negative electrode are transferred and reduced across the

molten salt electrolyte or positive electrode, forming a liquid metal alloy or intermetallic compound. The reverse process occurs for charging. The volume of the liquid metal electrodes changes based on whether the cell is charging or discharging. When the battery discharges, the positive liquid metal electrode decreases in volume and vice versa during charging.

Opposite to discharging, charging transfers electrons in the reverse direction to reactivate the material for reuse. The oxidation and reduction reactions that occur during discharging reverse directions during charging to restore the liquid metals to their original state. These reactions require specific materials to be used at both electrode and electrolyte layers.

Desirable electrode materials for liquid metal batteries have low operating temperatures (melting point < 1000°C, boiling point < 2500°C), are electrically conductive ($\sigma > 1 \text{ S cm}^{-1}$), and are inexpensive. The deposition potential of the liquid metal from the molten salt electrolyte is used to determine whether the electrode is positive ($> -1.0 \text{ V}$) or negative ($< -2.0 \text{ V}$).

Figure 13 shows the deposition potentials of various candidate metals per their location on the periodic table for liquid metal battery applications.

1																	18
H	2											13	14	15	16	17	He
Li	Be											B	C	N	O	F	Ne
Na	Mg	3	4	5	6	7	8	9	10	11	12	Al	Si	P	S	Cl	Ar
K	Ca	Sc	Ti	V	Cr	Mn	Fe	Co	Ni	Cu	Zn	Ga	Ge	As	Se	Br	Kr
Rb	Sr	Y	Zr	Nb	Mo	Tc	Ru	Rh	Pd	Ag	Cd	In	Sn	Sb	Te	I	Xe
Cs	Ba		Hf	Ta	W	Re	Os	Ir	Pt	Au	Hg	Tl	Pb	Bi	Po	At	Rn

Figure 13: Orange elements are negative electrode candidates. Green elements are positive electrode candidates.

Orange elements have deposition potentials less than -2.0 V making them negative electrode candidate materials. Positive electrode elements are highlighted in green with deposition potentials greater than -1.0 V (except aluminum at approximately -1.6 V). The greater the

difference in deposition potential the better the cell performs. This is based on the idea of pairing a strong electron donor metal with a strong electron acceptor metal.

Due to the abundant and inexpensive materials used, liquid metal batteries have the potential to be economically feasible options in the grid energy storage market (Sadoway, 2003).

Theoretically, molten metal batteries can achieve high life cycles suitable for the grid's demands. The self-sustaining nature of the cell allows it to store energy off the grid, even with intermittent energy sources such as wind power. The idea of a long lasting, renewable storage option for grid energy applications is promising.

Despite the advantages, liquid metal batteries are hindered by elevated operating temperatures ($> 200\text{ }^{\circ}\text{C}$), low theoretical specific energy densities ($< 200\text{ Wh kg}^{-1}$), low equilibrium cell voltages ($< 1.0\text{ V}$), corrosive materials and high discharge rates for some electrode pairs. The high operating temperature is costly and requires energy to be taken from another source and can lead to corrosion. The corrosiveness of the materials and operating temperatures factor into the low energy densities. Alloyed metals are an option to combat the issues that pure liquid metal batteries face.

2.5 Liquid Metal-Air Batteries

Liquid metal-air batteries are a recently proposed new type of battery that incorporates aspects of metal air batteries, liquid metal batteries, and flow batteries (Otaegui et al., 2014).

Fundamentally, these batteries solve the issues of low energy density, dendrite formation, and short life cycles by virtue of their composition. Typically, these batteries must be maintained at high temperatures, which limit the majority of their applications to stationary energy storage.

Because this system produces a metal oxide as part of its electrochemical reaction, these types of batteries should have a very high theoretical energy density, making them promising for storing energy. Moreover, because these batteries are composed of fluids, which avoids dendrite formation and ensures that the battery can still effectively function even when a certain part of the metal anode becomes electrically inert. Because of this property, liquid metal-air batteries can, in principle, be charged and discharged numerous times without destroying the battery, guaranteeing a long life cycle for the battery (Otaegui et al., 2014)

In an investigation, a liquid metal-air battery used liquid tin as the anode. The cathode and electrolyte layer were formed of $(\text{La}_{0.6}\text{Sr}_{0.4})_{0.95}\text{FeO}_{3-x}\text{-Ce}_{0.8}\text{Sm}_{0.2}\text{O}_{2-x}$ (LSF-SDC) composite and $(\text{ZrO}_2)_{0.97}(\text{Y}_2\text{O}_3)_{0.03}$ (3YSZ), respectively. When this battery was tested at 800°C , the discharging voltage was ~ 0.85 V. Additional testing showed that the general capacity of the cell remained fairly consistent over the course of nearly 1000 charge-discharge cycles (Otaegui et al., 2014). Based on these promising results, a new liquid metal-air battery is proposed here that operates at low temperatures.

2.5.1 Liquid Gallium Anode Potential

Liquid Gallium is one possible anode material candidate for a liquid metal-air battery because of its low melting point of 29.77°C . In addition to its low melting point, it presents no major safety issues, at worst causing “skin and eye irritation” (*Gallium*, 2010). While it is possible for it to be corrosive to alloys and metals—particularly aluminum—at elevated temperatures, lower temperatures are not an issue.

Aside from its low melting point, gallium is advantageous in that it easily forms oxides in aqueous alkaline solution. This demonstrates that gallium readily oxidizes due to a low activation energy barrier. However, the resulting oxide film will influence the electrochemistry, and depending on the pH, different ions may exist within the electrolyte, including $\text{Ga}(\text{OH})_4^-$ (Chung, 2013). Solid gallium is theoretically able to achieve a higher capacity due to its surface roughness, creating more active areas, but liquid gallium was found to be less inhibited than its solid counterpart. Additionally, the oxidation of liquid gallium occurs with little to no overpotential loss, allowing for better performance.

Although gallium has yet to be truly used in electrochemical energy storage, it has been important in different electrochemical applications. For instance gallium is included among the group 15 elements, which exhibit semiconducting properties (Moskalyk, 2003). Both gallium and its alloys, such as GaAs, GaN, InGaN, and $\text{Cu}(\text{InGa})\text{Se}_2$, have been used in semiconductors for microelectronics (Chung, 2013). Such applications include lasers, microwave transceivers, and light emitting diodes.

2.6 Electrochemical Reactions for Liquid Metal-Air Batteries

Reduction and oxidation (redox) reactions occur at a three phase interface consisting of the liquid metal electrode, electrolyte, and catalyst (Otaegui et al., 2014). A general schematic showing the reactions occurring within a liquid metal air battery is shown in Figure 14. The three phase interface and the electrode half-reactions are shown in a generic form. During discharge, the passage of ions through the electrolyte is enabled by the oxygen reduction reaction. Upon reaching the metal electrode, the metal oxidation reaction occurs releasing electrons to an external circuit. These redox reactions can be reversed for the recharging process

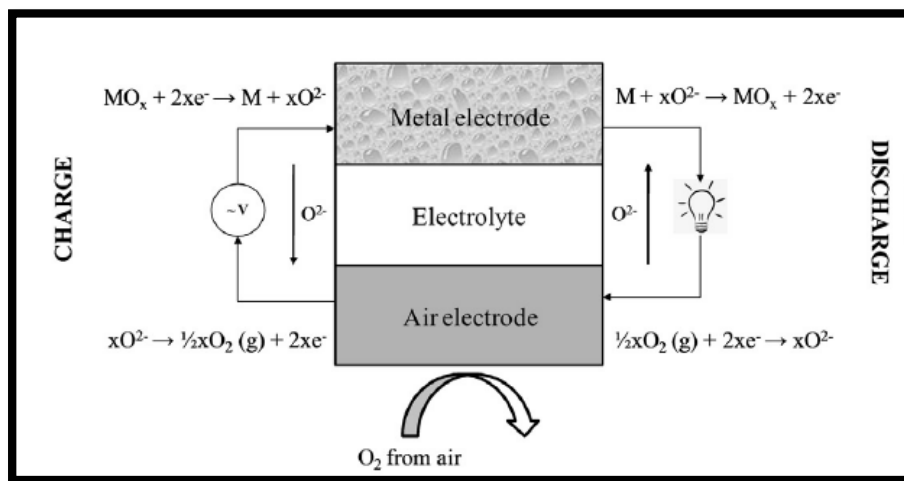


Figure 14: General high temperature liquid metal air battery schematic showing redox reactions during charging and discharging cycles (Otaegui et al., 2014).

2.6.1 Oxygen Reduction and Evolution Reaction

During discharge, oxygen from the atmosphere is reduced into ions by a catalyst bound to a porous gas diffusion membrane. Figure 15 shows this air cathode reaction schematically.

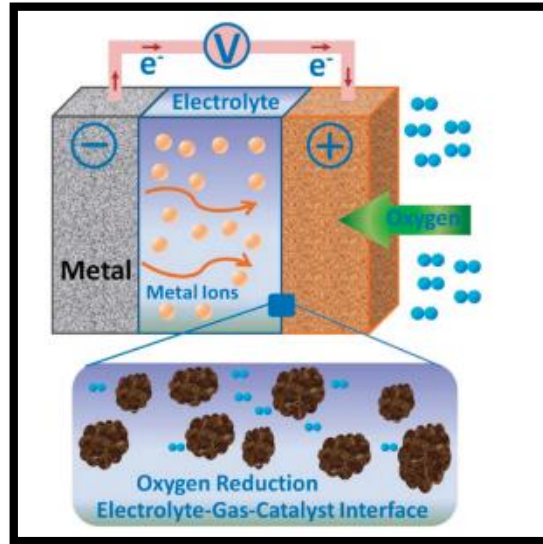
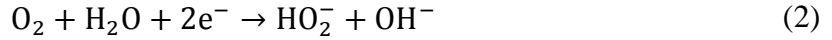
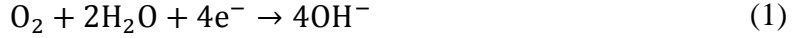


Figure 15: Schematic of oxygen reduction at porous gas diffusion membrane (Cheng and Chen, 2012)

Air electrodes are composed of three major components: a porous material, a binder, and a catalyst. The porous material, high surface area carbon, and the binder, polytetrafluoroethylene (PTFE), make up the gas diffusion layer (GDL). Porous carbon is used as a support for the catalyst, to provide electrical conductivity, and to diffuse oxygen (Cheng and Chen, 2012). The pores of the GDL provides sites for the catalyst and allows for the diffusion of oxygen. The pores function as a substrate for the catalyst to work at the triple interface of oxygen (gas), the electrolyte (liquid), and carbon (solid). If the pores are too small, they may become easily blocked, but if the pores are too large, the volumetric energy density will decrease (Lee et al., 2011). Higher surface area carbon materials have higher specific capacities as the surface area dictates the number of active sites in the electrode.

During discharge, there are a series of electrochemical reactions that reduce the oxygen. When charging, the reverse reaction occurs and oxygen is evolved. This series can occur via a two-electron or four-electron pathway, and catalytic materials affect the pathway and mechanisms that occur. For instance, generally the catalyst will cleave the oxygen-oxygen bond, but in the

case of the EMD catalyst studied by Cheng and Chen (2012), the bond was not cleaved, and rather the catalyst reduced O_2 to O_2^{2-} . Very often, the catalyst used is platinum or manganese dioxide to improve the typical sluggish reaction kinetics. The general four-electron pathway of the oxygen reduction and evolution reaction with alkaline electrolyte is shown below:



2.6.2 Liquid Metal Electrode Oxidation and Reduction in Alkaline Media

During discharge, hydroxide ions from the oxygen reduction reaction transport to the liquid metal electrode through an ion conducting electrolyte. Porous separator material such as polymer, alumina, or zirconia cloth can be soaked in aqueous electrolyte solution to form the separator electrolyte layer that allows hydroxide ion transport. The liquid metal oxidizes upon contact with hydroxyl ions when discharging, releasing electrons to a current collector flowing through an external circuit. This redox reaction scheme is theoretically reversible for some liquid metal air batteries chemistries. For the charging process, the oxidized liquid metal is reduced to its original state, reversing the discharge cycle.

In the case where gallium is the liquid metal and the electrolyte is an alkaline solution, oxidation products such as Ga_2O_3 and $Ga(OH)_3$ form on the surface when discharging (Perkins, 1973). X-ray diffraction studies show that the passivating layer on the gallium surface is approximately 0.7 nm thick and most likely composed of both $Ga(OH)_3$ and Ga_2O_3 (Regan, 1997). Tetrahydroxyl gallate anions, $Ga(OH)_4^-$, form in solution with strong alkaline media (Gladyshev et al., 2013). Figure 16: Pourbaix diagram for gallium. Dashed line represents thermodynamically stable region (Schweitzer, 2009). Figure 16 shows a Pourbaix diagram for Gallium (Schweitzer, 2009). At a pH magnitude of 14 or greater, tetrahydroxyl gallate anions are the likely species due to thermodynamic stability.

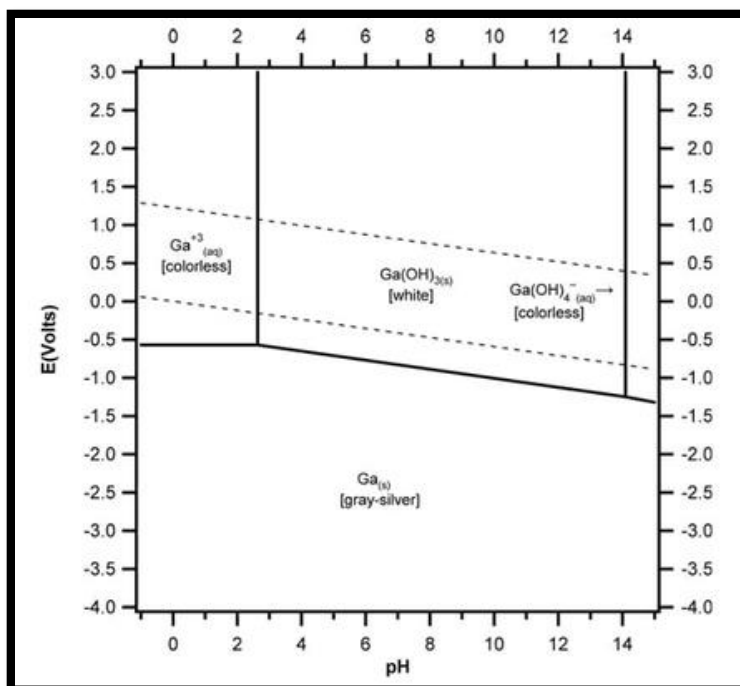
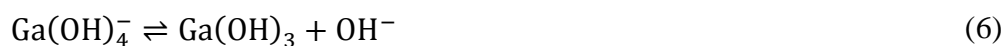


Figure 16: Pourbaix diagram for gallium. Dashed line represents thermodynamically stable region (Schweitzer, 2009).

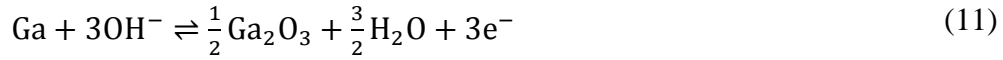
When these gallate products form, electrons are released from the gallium surface and transport through an external circuit to the air cathode. Once reaction solubility reaches equilibrium, the oxide and hydroxide species are hypothesized to form. The reverse electron flow occurs during charging. The reversible reaction schemes for the oxidation of gallium in alkaline media are shown below:

For the formation and dissolution of gallium hydroxide:



For the formation and dissolution of gallium oxide:





The oxidation reactions create an electrical charge, or current, and the potential difference between two electrodes is the usable voltage for an external load. However, the potentially passivating layer of oxidation products on the gallium surface could inhibit further reaction over time. In general, as reaction sites decrease with an increasing passivating layer, the voltage of the cell additionally decreases. The passivating layer could eventually cause the electrical circuit to decrease to a cut-off voltage. An electrical current can later be supplied to the circuit by recharging for regeneration of the liquid metal fuel.

3 Methodology

3.1 Design of the Battery

A modified version of the Li-air Swagelok cell of the type reported by Beattie et al. (2009) was used for Ga-air testing. The exploded and collapsed view of the prototype Ga-air cell is shown in Figure 17.

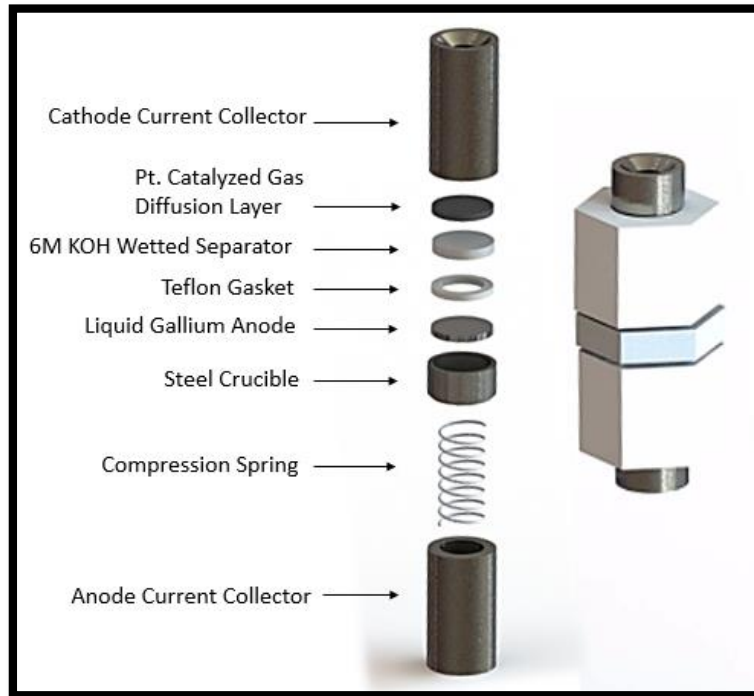


Figure 17: Exploded view (left) and collapsed view (right) of the Swagelok Ga-air cell design

3.2 Materials

The materials used to construct the Ga-air cell were non-toxic and environmentally friendly. These components are organized in subsequent sections by mechanical parts, anode, electrolyte wetted separators, and cathode materials.

3.2.1 Mechanical Parts

The mechanical parts of this battery design are listed below:

Current collectors:

- Two stainless steel node current collectors, manufactured by Target Machine (Figure 18)
- Stainless steel crucible machined by WPI Unit Operations Lab.

- McMaster Carr 302 Stainless Steel Precision Compression Spring (0.750 in long, 0.36 in O.D., 0.026 in thick wire).

Encasing:

- PTFE Swagelok Tube Fitting with Ferrules, Union, 1/2 in. Tube OD.

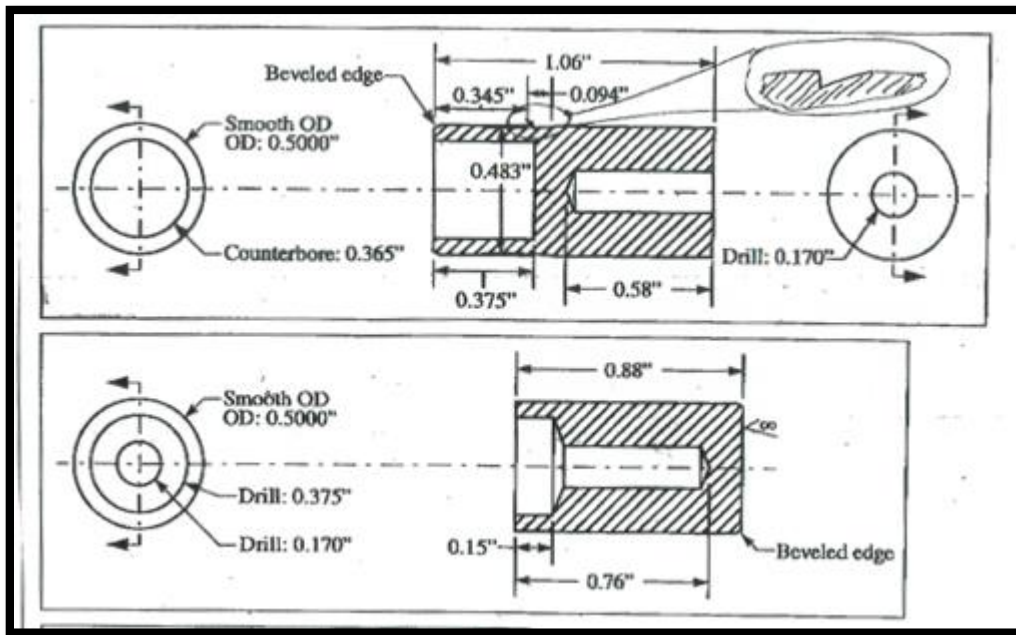


Figure 18: Stainless steel electrode current collector mechanical drawings. Anode (top), cathode (bottom).

3.2.2 Liquid Metal Anode

Pure liquid gallium was chosen for the anode material for this battery; this metal was chosen for its non-toxicity, increased reactivity, potential reversibility, self-healing properties, and low melting point (29.77 °C). Increased reactivity will enable battery spontaneity, which is desirable for low-maintenance batteries. Good reversibility is desirable to ensure the continued use of the battery. Self-healing properties are a significant asset to ensure a battery is low-maintenance since the liquid metal will naturally correct improper surface contact or oxide build-up and has no memory effect. Low melting point is essential for ease of testing the concept, but in tangential applications this may become a less important property.

3.2.3 Electrolyte and Separator

The baseline electrolyte used in this system is a 33.6 wt.% potassium hydroxide solution (6M KOH). At this concentration, KOH has been found to have a high conductivity and promote the formation of gallium tetrahydroxyl gallate ions. This electrolyte is held by capillary action in a separator placed between both electrodes to prevent short circuiting. Previous studies on metal-air batteries used solid yttria-stabilized zirconia as the electrolyte separator material. Zircar woven cloth type ZYK-15 (yttria-stabilized zirconia) was used for the Ga-air cell.

Potassium hydroxide, like other alkaline solutions, is susceptible to carbonation when exposed to ambient carbon dioxide. To test this issue, an anion exchange membrane (AEM) from Membrane International, model AMI-7001S, was also used as a separator material. The AEM consists of a long chain polymer to counteract the time of carbonation (Vega et al., 2010).

3.2.4 Air Cathode

The cathode fuel used for this investigation was oxygen from ambient air. Most tests were conducted simply using ambient air; however, some results were obtained using pure oxygen for comparative purposes.

This air cathode assembly consisted of a catalyzed gas diffusion layer (GDL) to allow for the reduction and evolution of oxygen from air. The GDL used consists of a layer of graphitized carbon coated in a fine platinum catalyst. Oxygen can bind to the platinum catalyst layer to release 4 electrons at an improved reaction rate compared to MnO_2 catalyst, which is a cheaper alternative but effective mostly for 2 electron transfer.

3.3 Electrochemical Cell Set Up and Testing

The Ga-air cell was assembled on a benchtop located in WPI's Fuel Cell Laboratory. The assembly followed the three layer cell design (anode, electrolyte, and cathode) within a PTFE Swagelok fitting (Figure 17). A more detailed list of procedures is included within Appendices A-C with a photographic guide found in Appendix D.

The cell was assembled from the anode to the cathode. About 1.2 grams of gallium was melted and put into the crucible. After that, a Teflon gasket was layered on top of the crucible to ensure sealing and to prevent the gallium from leaking. The Teflon gasket was manufactured using two

hole punches: one with the same outer diameter of the crucible and the other with a smaller diameter to allow contact between the gallium and the electrolyte. Next, the KOH soaked separator was placed on top of the gasket, and finally the GDL was placed on the separator with the catalyzed side down and in contact with the electrolyte. The cathode current collector node was then screwed on to the PTFE union to guarantee proper contact between layers. The two separators used in this case were zirconia cloth and an anion exchange membrane (AEM). An additional set up was included for pure oxygen feed tests.

Although an oven was used for tests greater than 80°C, a heating lamp was generally used for the tests as it provided more uniform heating, while the temperature in the furnace fluctuated (Figure 19). The heating lamp allowed for the temperature to range from 30°C to 80°C. The temperature was adjusted by moving the cell closer to or further away from the lamp and by using a temperature probe to measure the temperature. The cell was placed in a ring stand with the cathode side facing down to ensure good contact between the layers (Figure 20). The cell was clamped in the ring stand for 5 to 10 minutes prior to testing to be sure that the gallium would be liquid.

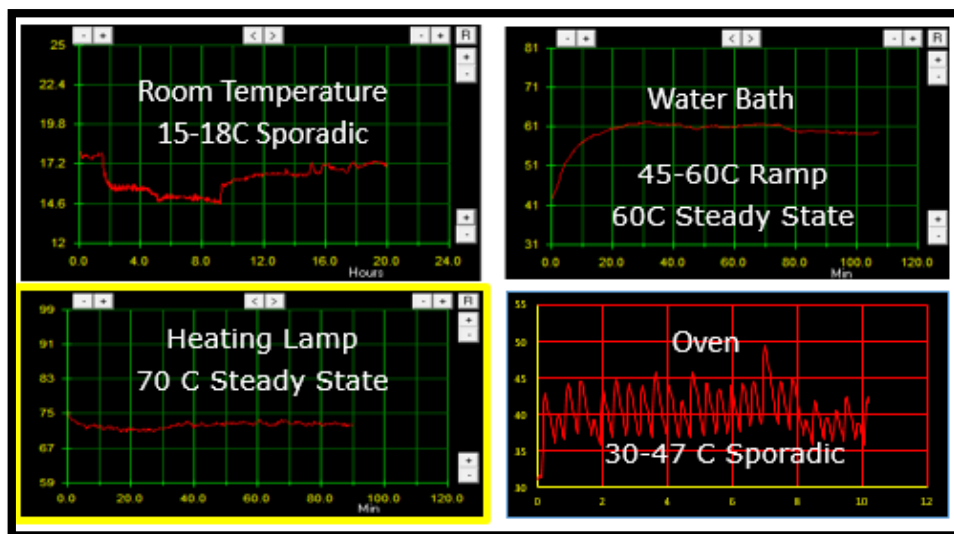


Figure 19: Heating instruments tested with their respective temperature profiles.

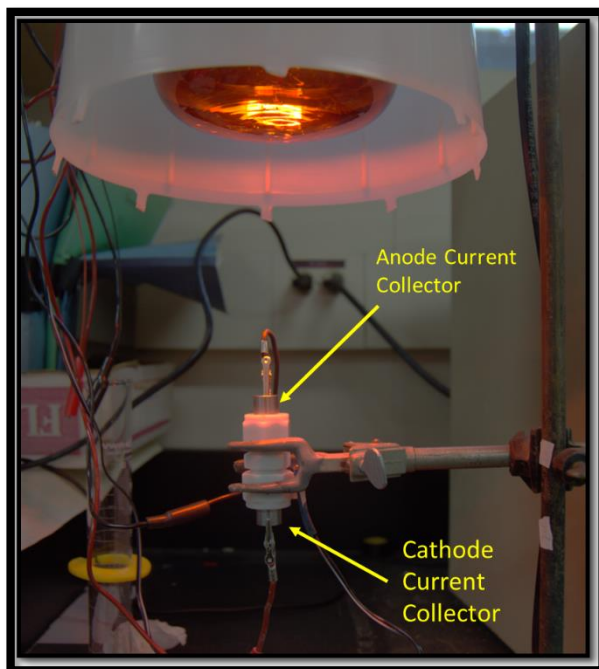


Figure 20: Ring stand and heating lamp set up with cell orientation shown.

When the oven was used, the set up was similar however a ring stand was placed inside the oven with the leads entering through holes at the top. The oven, due to the nature of its control system, was sporadic in regards to temperature, therefore the heating lamp was the preferred method of heating.

3.3.1 Zirconia Cloth Electrolyte Fabrication

Zirconia cloth type ZYK-15 manufactured by Zircar Zirconia, Inc. was cut to a defined specification and wetted with 33.6 wt.% KOH. The separator was first cut using a metal punch with a diameter of 11.8mm. Then the cut zirconia paper was soaked for 20 minutes in 33.6 wt.% KOH solution. The solution was covered throughout the 20 minute soaking period to prevent premature carbonation of the KOH. The step-by-step procedure is described in Appendix B: Electrolyte Procedure

3.3.2 Anion Exchange Membrane Procedure

To determine the potential effect of carbonation of the KOH electrolyte, tests using an anion exchange membrane (AEM), manufactured by Membrane International model AMI-7001S, were also conducted. The AEM, like the zirconia paper, was cut to the same size using a punch and

was soaked in a 33.6 wt.% KOH solution. The AEM, based on required preparation technique, was soaked for over 24 hours in the alkaline electrolyte prior to assembly and testing. After the initial soaking, both sides of the AEM was rinsed using deionized water and then wetted with a few drops of 33.6 wt.% KOH solution. Then the separator was applied to the cell in the same manner as the zirconia cloth. A more detailed step by step procedure is available in Appendix B: Electrolyte Procedure

3.3.3 Pure Oxygen Testing

Pure oxygen tests were set up by connecting an oxygen tank to tubing that led to the air cathode of the assembled cell. A needle valve was included in order to more precisely adjust the flow. Further tubing was connected with an inner diameter of 2mm. This small diameter allowed for the tubing to fit into the open part of the cathode node of the Swagelok cell to directly flow oxygen into the cathode. This set up provided enough room for the leads to be attached to the cell so measurements could be taken.

3.4 Battery Analyzer Testing Procedure (BAWIN500 Program)

All testing was performed on a modified version of Battery Metric's MC2020 model. This model was specifically customized such that it could precisely discharge and charge the batteries at low currents (0.1mA/1mA/10mA). The software used in tandem with this model was Battery Metric's BAWIN500 program. Exact details for these procedures and screenshots can be found in Appendix E.

3.4.1 Polarization Testing

Polarization curves were obtained by loading a saved customizable program. This program was designed to perform a galvanostaircase polarization, where current is increased in a step-wise manner for a brief period of time. The battery was discharged over a range of currents from 0 to 15 mA. Each step discharged the cell for 20s with data points logged every 10 seconds. The steps increased in 0.1 mA increments until 7 mA was reached and then the current was increased in 0.5 mA increments until it reached 15 mA. In this case, the cut off voltage was set to 0.001V to allow for the full range of currents to be tested.

3.4.2 Discharge Testing

Similar to the polarization testing, a program was set up to run discharge tests. The discharge tests allowed for a 2 minute initial pause period in order to get an average OCV and then the program would drain a 0.5 mA current from the cell until the cell voltage reached a 0.3 V cutoff. This test was often completed after performing a polarization test in order to achieve each type of test for a specified set of conditions.

4 Results

4.1 Theoretical Calculations

4.1.1 Open Circuit Voltage

The theoretical open circuit voltage (V^0) of an electrochemical reaction can be determined by its thermodynamic standard Gibbs free energy as shown in Equation 12. This is an indication of the theoretical potential with no supplied current.

$$\Delta G^0 = -nFV_{rxn}^0 \quad (12)$$

This relationship involves the number of electrons, n , that are transferred and Faraday's constant, F . In the case of gallium oxidation and reduction in alkaline media, three electrons are transferred. Using the reactions described in Section 2.6.2, the theoretical open circuit voltages of potential overall reactions are shown in Table 1 and Table 2.

Table 1: Open Circuit Voltage Calculation for the Formation of a Ga-Air Battery Assuming Gallium Hydroxide is Formed.

Electrode	Reaction	Potential (V)	ΔG^0 (kJ/mol)
Anode	$\text{Ga} + 4\text{OH}^- \rightleftharpoons \text{Ga}(\text{OH})_4^- + 3\text{e}^-$		
Anode	$\text{Ga}(\text{OH})_4^- \rightleftharpoons \text{Ga}(\text{OH})_3 + \text{OH}^-$		
Overall Anode	$\text{Ga} + 3\text{OH}^- \rightleftharpoons \text{Ga}(\text{OH})_3 + 3\text{e}^-$	$V_A^0 = -1.242$	-360
Cathode	$\text{O}_2 + 2\text{H}_2\text{O} + 4\text{e}^- \rightleftharpoons 4\text{OH}^-$	$V_C^0 = +0.401$	-155
Overall	$\text{Ga} + \frac{3}{4}\text{O}_2 + \frac{3}{2}\text{H}_2\text{O} \rightleftharpoons \text{Ga}(\text{OH})_3$	$V^0 = V_C^0 - V_A^0$ $V^0 = 1.643 \text{ V}$	-476

Table 2: Open Circuit Voltage Calculation for the Formation of a Ga-Air Battery Assuming Gallium Oxide is Formed.

Electrode	Reaction	Potential	ΔG^0 (kJ/mol)
Anode	$\text{Ga} + 4\text{OH}^- \rightleftharpoons \text{Ga}(\text{OH})_4^- + 3\text{e}^-$		
Anode	$\text{Ga}(\text{OH})_4^- \rightleftharpoons \text{Ga}(\text{OH})_3 + \text{OH}^-$		
Anode	$\text{Ga}(\text{OH})_3 \rightleftharpoons \text{Ga}_2\text{O}_3 + 3\text{H}_2\text{O}$		
Overall Anode	$\text{Ga} + 3\text{OH}^- \rightleftharpoons \frac{1}{2}\text{Ga}_2\text{O}_3 + \frac{3}{2}\text{H}_2\text{O} + 3\text{e}^-$	$V_A^0 = -1.323$	-383
Cathode	$\text{O}_2 + 2\text{H}_2\text{O} + 4\text{e}^- \rightleftharpoons 4\text{OH}^-$	$V_C^0 = +0.401$	-155
Overall	$\text{Ga} + \frac{3}{4}\text{O}_2 \rightleftharpoons \frac{1}{2}\text{Ga}_2\text{O}_3$	$V^0 = V_c^0 - V_a^0$ $V^0 = 1.724 \text{ V}$	-499

The overall anode reaction to form gallium hydroxide has a somewhat lower theoretical potential and Gibbs free energy than the formation of gallium oxide. However, it is not clear whether hydroxide or oxide is the final product of the cell discharge reaction. Nevertheless, it is still possible to form gallium oxide as shown in literature review. For this reason both species are considered possible gallium oxidation products here.

The theoretical open circuit potential of Ga-air compares well with the commercial Zn-air battery. The cell reactions that take place in a Zn-air battery with their respective OCVs are shown in Table 3. Note that zinc involves only two electrons as opposed to three for gallium.

Table 3: Open Circuit Voltage Calculation for a Zn-Air Battery.

Electrode	Reaction	Potential	ΔG^0 (kJ/mol)
Anode	$Zn + 4OH^- \rightleftharpoons Zn(OH)_4^{2-} + 2e^-$		
Anode	$Zn(OH)_4^{2-} \rightleftharpoons ZnO + H_2O + 2OH^-$		
Overall Anode	$Zn + 2OH^- \rightleftharpoons ZnO + H_2O + 2e^-$	$V_A^0 = -1.260$	-243
Cathode	$\frac{1}{2}O_2 + H_2O + 2e^- \rightleftharpoons 2OH^-$	$V_C^0 = +0.401$	-155
Overall	$\frac{1}{2}O_2 + Zn \rightleftharpoons ZnO$	$V^0 = V_C^0 - V_A^0$ $V^0 = 1.6661 V$	-321

4.1.2 Electrochemical Equivalent, Capacity and Service Life

The theoretical electrochemical equivalent of a material is a measure of the available ampere hours in an electrochemical cell. The electrochemical equivalent of the anode material is typically used in metal air battery calculations and is determined by Equation 13. As a result, Zn-air batteries have a theoretical electrochemical equivalent of 820 mAh/s while Ga-air batteries have an improved 1150 mAh/s.

$$E_Q = \frac{nF}{3600 * MW_{anode}} \left[\frac{Ah}{g} \right] \quad (13)$$

The theoretical capacity, Q, of a battery in terms of mAh can be calculated by multiplying E_Q by the weight of the anode material used. By taking 1.2 g as an example, the capacity of a Zn-air cell would be 984 mAh while the capacity of a Ga-air cell would be 1,384 mAh. Using the capacity in terms of mAh allows for the calculation of theoretical discharge service life by Equation 14.

$$t = \text{Discharge service Life [h]} = \frac{Q[\text{mAh}]}{\text{discharge current [mA]}} \quad (14)$$

Thus, for a 1 mA constant discharge current, the theoretical discharge service life of a Zn-air battery with 1.2 g of zinc anode material would be 984 hours. By contrast, the theoretical discharge service life of a Ga-air battery under the same conditions would be 1384 hours, a 40% increase.

4.1.3 Gravimetric and Volumetric Energy Density

The gravimetric energy density of a battery indicates the amount of energy that can be discharged per unit mass of material, while volumetric energy density is a measure of energy per unit volume. Metal air batteries have the highest theoretical gravimetric and volumetric energy densities because of their use of atmospheric air as a cathode reactant. Air electrodes take up very little space or weight and there is a constant supply of fresh air that does not deplete over time like other cathode materials. To calculate the theoretical gravimetric energy of a metal air battery, the anode material is the only component considered as shown by Equation 15. By multiplying this value by the density of the anode material, the theoretical volumetric energy density is obtained. A comparison of Ga-air to Zn-air is shown in Table 4.

$$\text{Gravimetric Energy Density} \left[\frac{\text{Wh}}{\text{kg}} \right] = V_0 [\text{V}] * E_{Q,\text{anode}} \left[\frac{\text{Ah}}{\text{g}} \right] * 1000 \left[\frac{\text{g}}{\text{kg}} \right] \quad (15)$$

Table 4: Theoretical Energy Density Comparison of Ga-air and Zn-air Batteries.

Electrochemical System	Gravimetric Energy Density (Wh/kg)	Volumetric Energy Density (Wh/L)
Zn-air	1,361	9,723
Ga-air (gallium hydroxide)	1,895	11,549
Ga-air (gallium oxide)	1,989	12,121

It is clear that gallium-air battery is potentially very attractive. In either case of hydroxide or oxide formation, the gallium-air battery has a larger energy density compared to zinc.

4.2 Open Circuit Voltage (OCV) Results

4.2.1 Average OCV Testing Results

Before each discharge test, an average OCV for the liquid gallium-air cell was obtained. The OCV was obtained under four different sets of conditions depending on the electrolyte layer (zirconia cloth or anion exchange membrane), heating method and temperature (heat lamp or oven), and oxygen feed (air or pure oxygen). These different conditions created the four different conditions in accordance with Table 5.

Table 5: Conditions for OCV results

Condition	Electrolyte Layer	Heating Method	Oxygen Feed
Condition 1	Zirconia Cloth	Heat Lamp	Air
Condition 2	Anion Exchange Membrane	Heat Lamp	Air
Condition 3	Zirconia Cloth	Oven	Air
Condition 4	Zirconia Cloth	Heat Lamp	Pure Oxygen

Given a natural variation in the temperature of each result, the average OCV was calculated alongside an average temperature, both with standard deviations included. The calculated average OCV's and the corresponding temperatures are summarized in Table 6.

Table 6: OCV Test Results

Condition	Temperature (°C)	OCV (V)
Condition 1	57.7 ± 6.3	1.157 ± 0.032
Condition 2	41.4 ± 14.1	1.155 ± 0.032
Condition 3	102.7 ± 12.0	1.292 ± 0.037
Condition 4	41.2 ± 15.3	1.136 ± 0.034

As seen in Table 6, most of the OCV's were fairly consistent as long as the temperature also remained consistent. This was observed for conditions 1, 2, and 4, which implies that the use of an anion exchange membrane over zirconia cloth will not increase OCV. Moreover, it demonstrates that a pure oxygen feed holds no advantages over ambient conditions in terms of OCV. However, condition 3 demonstrated that increasing the temperature has a notable increase in the OCV, as demonstrated in Figure 21.

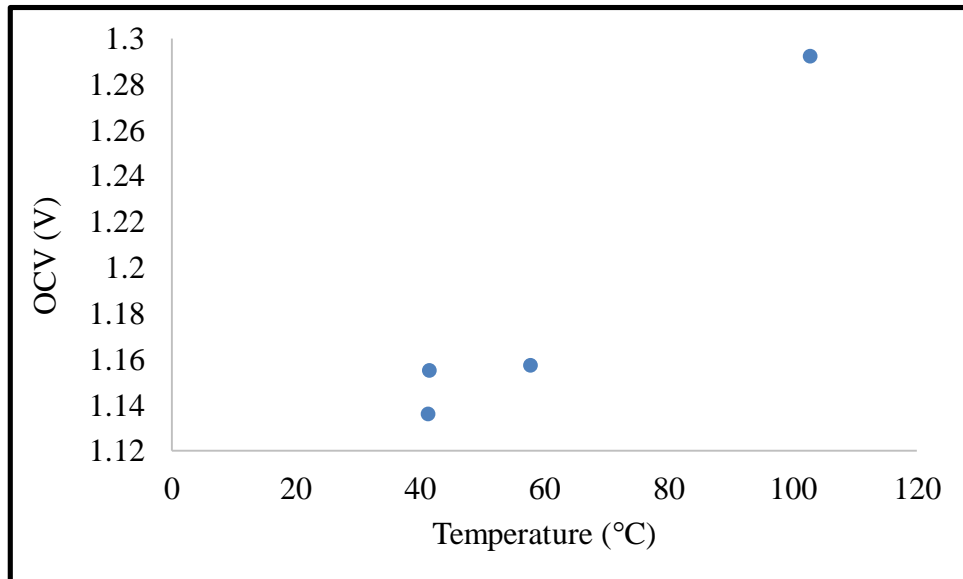


Figure 21: OCV vs Temperature

After a successful discharge of the cell, attempts to extend the total discharge time were performed by either shaking the cell or re-wetting the electrolyte layer with water. Before another discharge curve was generated, another OCV was measured before a load was applied to the cell. These attempts had some successes for conditions 1, 2, and 4; however, these methods were not attempted for condition 3. For condition 1, shaking was performed twice, resulting in a 5.8% drop from the initial conditions and a 9.9% drop from the first shake; this corresponds to a change in OCV from 1.196 V to 1.127 V to 1.015 V. For condition 2, shaking was performed once, resulting in a 0.2% drop from the initial conditions; this corresponds to a change in OCV from 1.195 V to 1.193 V. For condition 3, shaking followed by re-wetting was performed, resulting in a 19.8% drop from initial conditions and a 20.5% increase from the first shake; this corresponds to a change in OCV from 1.172 V to 0.94 V to 1.133 V.

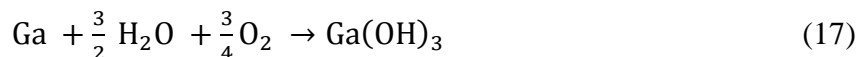
While shaking this cell revived it, the effect was short lived. This implies either that oxide formation on the separator is not inhibiting cell performance or that shaking the cell is not a rigorous enough procedure to remove the oxide layer. However, re-wetting was found to have a dramatic improvement on OCV results, which implies that separator drying plays an important role in the decline of the cell performance.

4.2.2 Experimental OCV Comparison to Theoretical

There are two overall reactions that gallium can undergo in the presence of air and an aqueous electrolyte. The first reaction forms gallium oxide (Ga_2O_3) in the presence of air. Its reaction is as follows:



The other reaction forms gallium hydroxide ($\text{Ga}(\text{OH})_3$) in the presence of water and oxygen in the following reaction:



For reaction 16, the theoretical OCV was calculated to be 1.724 V here, whereas the theoretical OCV for reaction 17 was calculated to be 1.643 V. Compared to the experimental results of 1.157 V, 1.155 V, 1.292 V, and 1.136 V for Conditions 1-4, the theoretical OCV's are higher, as expected. If the overall reaction is assumed to be reaction 16, then the OCV is 25 to 35% lower.

However, if the reaction is assumed to proceed according to reaction 17, the OCV is 20 to 30% lower. This discrepancy between the thermodynamic voltage and OCV is also observed in the Zn-air cell and is due to overpotentials due to polarization losses.

4.3 Polarization Testing

Galvanostaircase polarization (GSCP) tests were conducted to evaluate cell performance under various current loads. GSCP testing involves increasing the current in stepwise increments and measuring potential to achieve a polarization plot. Polarization curves and Tafel plots were generated for further analysis.

4.3.1 Polarization Plots

A polarization plot was created for a cell configuration with a 33.6 wt.% KOH wetted zirconia cloth separator at 50 °C as shown in Figure 22.

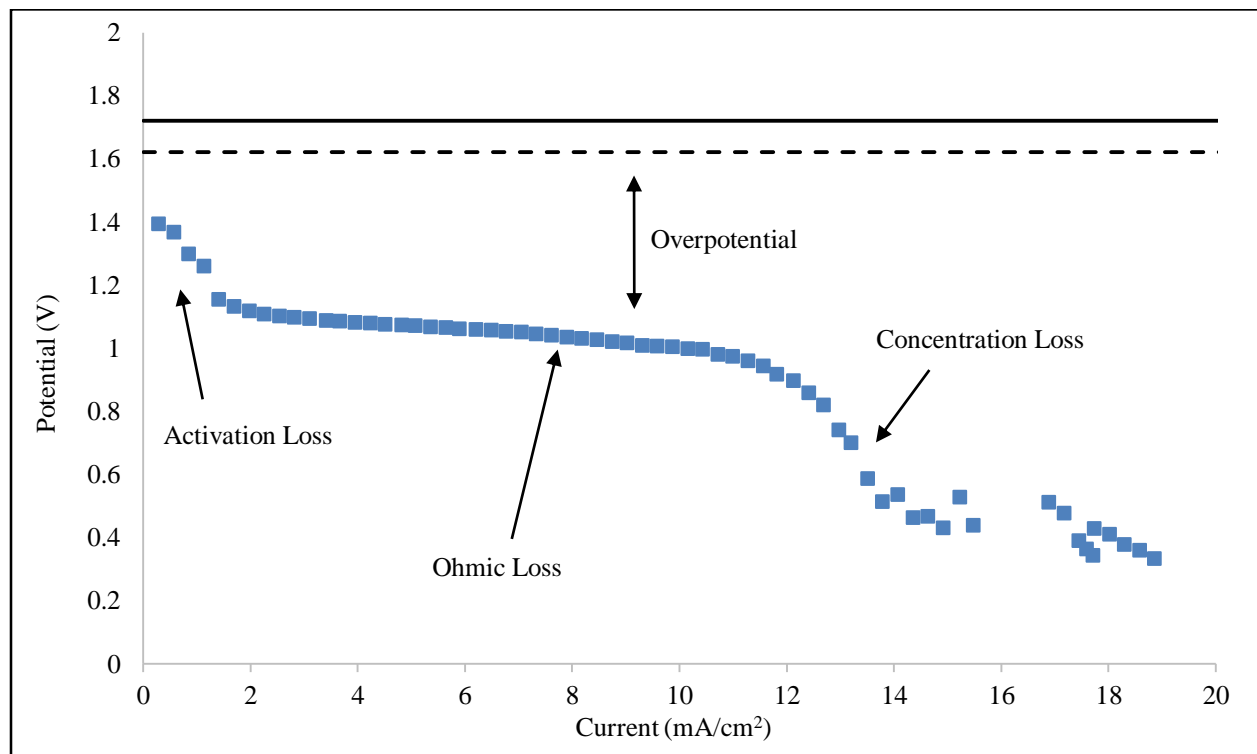


Figure 22: Polarization performance of Ga-air cell with zirconia cloth wetted with aqueous 33.6 wt.% KOH electrolyte at 40 °C. Theoretical OCV for Ga_2O_3 (solid black line) = 1.724 V. Theoretical OCV for $Ga(OH)_3$ (broken black line) = 1.643 V.

The polarization plot shows various regions where overpotential occurred from activation, ohmic and concentration losses. The overpotential is simply the difference between the theoretical and

measured potential, and account for potential losses or irreversibilities within the cell. Both Ga_2O_3 and $\text{Ga}(\text{OH})_3$ theoretical OCV values are shown because of uncertainty of overall reaction.

Activation losses were noticed at initial low current densities, less than 1.5 mA/cm^2 . The activation losses are those associated with electron transfer reaction kinetics during gallium oxidation and oxygen reduction reactions, requiring overpotential to enhance electrode kinetics to support the current load. In theory, lower current density means slower kinetics and lowers activation overpotential. The oxygen reduction reaction at the catalyzed GDL has been reported to and believed to have imposed a large portion of the activation overpotential here due to its sluggish kinetics. Although expensive, the platinum catalyst coating on the GDL provides a lower activation overpotential in comparison to other oxygen reducing catalyst materials such as MnO_2 , and is suitable for the reverse reaction needed in recharging. Since this study is concerned with feasibility, the optimization of the oxygen reduction reaction catalyst is beyond the scope of this work.

Loss associated with the internal resistance (IR) of the electrolyte caused a relatively flat ohmic overpotential region. Theoretically, ionic resistance and electronic resistance of the battery caused the IR drop. Ionic resistance is a factor of electrolyte conductivity, ion mobility and electrode surface area while electronic resistance is related to electrical contact of component materials. Although ohmic overpotential is inevitable, it can be reduced by improved electrolyte conductivity and electrical contact.

The concentration overpotential region was observed at the higher current densities. At this limiting current density, the electroactive species near the electrodes are consumed at a rate needed to support the current. Due to the increased consumption needed, the concentration of electrode material decreases and results in an overpotential loss. During discharge, the oxygen anion bulk concentration undergoes mass transport through the electrolyte and diffuses across the gallium oxide layer adjacent to the electrolyte layer at a limiting rate dependent on thickness and porosity. Thus, the overpotential region at high current densities may be regarded as diffusion limited because of this phenomenon.

Polarization plots at two different temperatures are shown in Figure 23. Thus, there was no discernable difference in polarization curves at the two different temperatures. The activation and ohmic overpotential regions were very similar in all aspects. The concentration overpotential region was not encountered in either case.

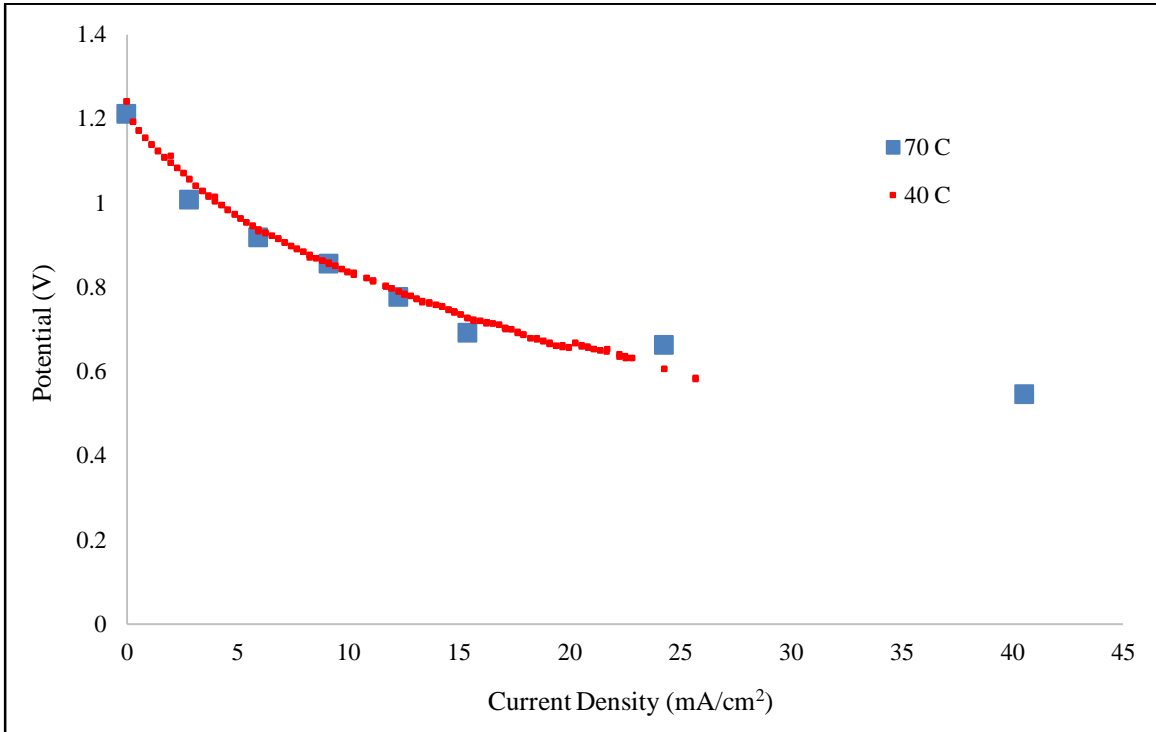


Figure 23: Polarization comparison for Ga-air cells with wetted zirconia cloth at 40 °C and 75 °C.

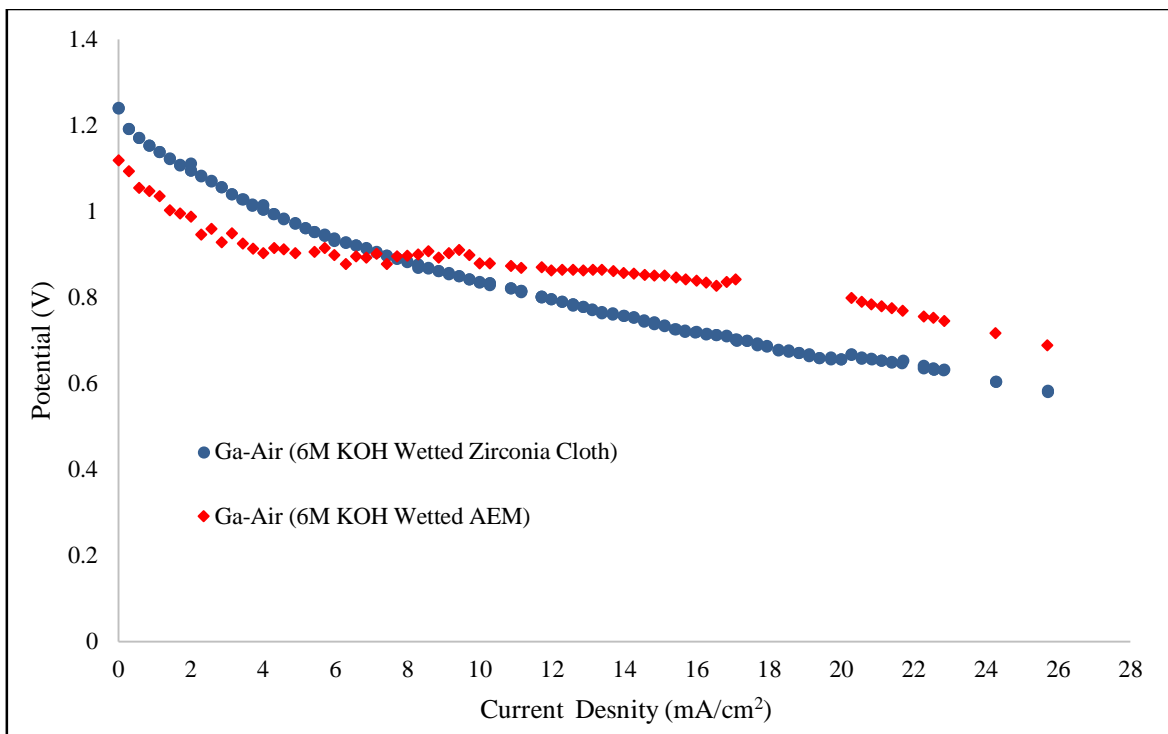


Figure 24: Polarization comparison for Ga-air cells with wetted zirconia cloth and anion exchange membrane (AEM) assemblies at 50 °C.

Polarizations curves for Ga-air cells with different electrolyte configurations, namely zirconia cloth versus AEM, are shown in Figure 24. Although very similar, the Ga-air cell performed better at higher current densities ($> 8\text{mA/cm}^2$) with an anion exchange membrane (AEM) soaked in 33.6 wt.% KOH electrolyte in comparison to the KOH wetted zirconia cloth. This could be a result of the AEM's ability to inhibit carbonation of the electrolyte or reduce drying. Carbon dioxide molecules can react with potassium hydroxide to form potassium carbonate, which can clog the pores of the separator. Therefore, the available OH^- ions become depleted and the potential decreases. A similar reduction in ions available for charge transfer occurs when the electrolyte layer dries up, leaving behind solid KOH.

Additional polarization curves (Figure 25) were generated for a commercial Zn-air button cell for comparative purposes.

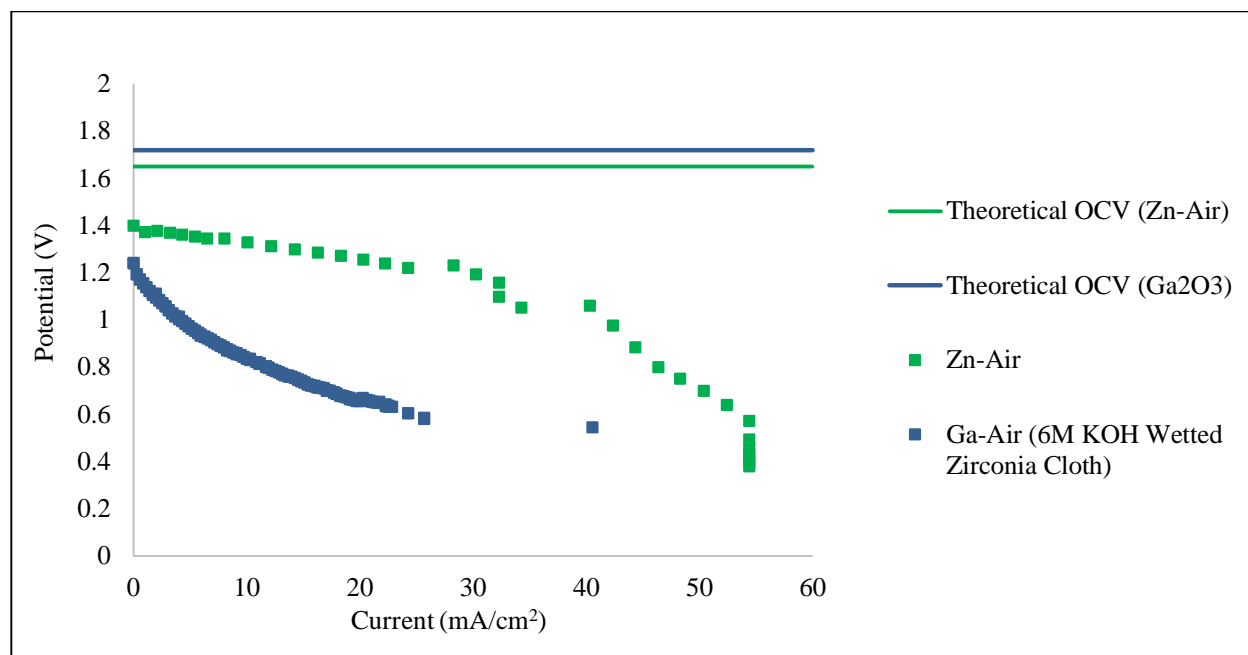


Figure 25: Polarization curves for a commercial Zn-Air cell, a Ga-Air cell with a zirconia separator, and a Ga-Air cell with an AEM.

The commercial Zn-air battery outperformed Ga-air in all aspects likely because of its superior electroactive material utilization. A zinc powder is mixed with gelled KOH electrolyte material in the anode compartment, allowing for maximum contact in three dimensions, so that active electrochemical area is substantially greater than the geometric cell area. The depletion of material to reach the mass transfer limited region would theoretically take longer in this configuration in comparison to the Ga-air cell. A flat two dimensional contact region between the liquid gallium metal surface and the wetted separator is much less in comparison. The top surface layer of gallium (0.35 cm² geometric area) can be fully utilized at higher current densities while the remaining active material would be largely unused. In a flow battery set up, this issue could be reduced as active gallium anode slurry could be circulated into the system.

4.3.2 Tafel Plots

Tafel plots were generated experimentally to evaluate the kinetic parameters of the electrochemical reactions during discharge. Because the gallium oxidation product and hence the thermodynamic voltage, is unknown, the overpotential was calculated for the two different thermodynamic potentials. The resulting Tafel plots of the standard cell configuration with zirconia cloth wetted with 33.6 wt.% KOH are shown in Figure 26.

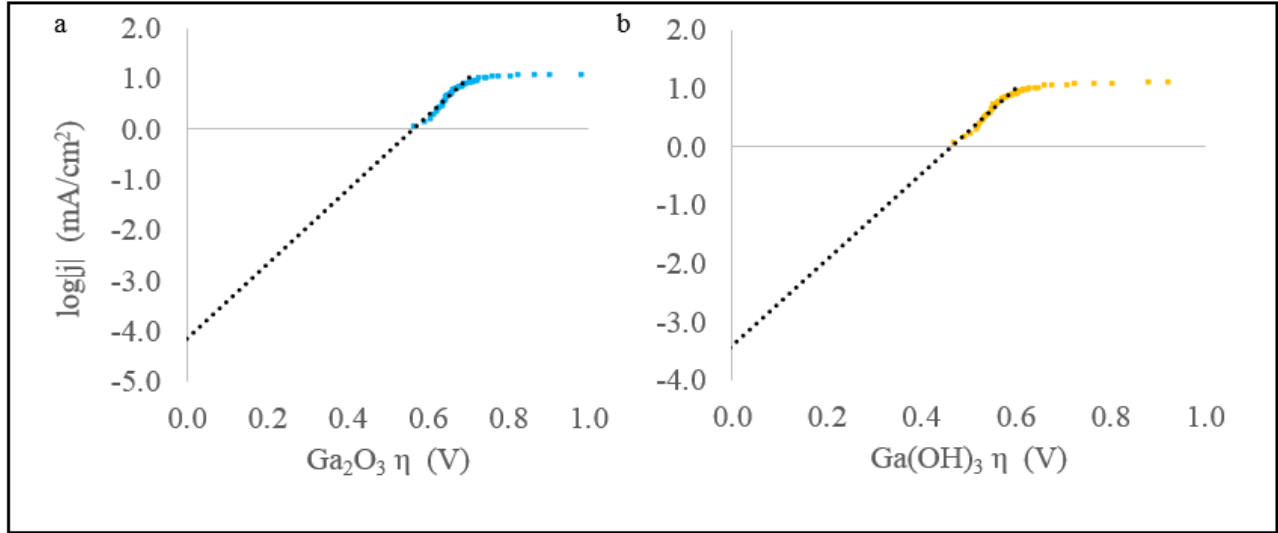


Figure 26: Tafel plots for Ga-air cell with 33.6 wt.% KOH wetted zirconia cloth at 65 °C. Overpotential shown for gallium oxide (a) and gallium hydroxide (b).

At low overpotentials, the Tafel plots exhibited a fairly linear region with an R^2 value of 0.97. For both linear regions, Tafel slopes were extrapolated to zero overpotential to obtain the exchange current density, i_0 . This is the effective current density where the forward and reverse reactions are equal and can be used for modeling. The slopes were then used to find the kinetic parameter defined as the anodic charge transfer coefficient, α_A , which is related to the overpotential needed to increase the reaction rate. Additional Tafel plots were created for the Ga-air cell configured with an anion exchange membrane to achieve a linear region of 0.95 R^2 shown in Figure 27. The resultant kinetic parameter values are tabulated in Table 7.

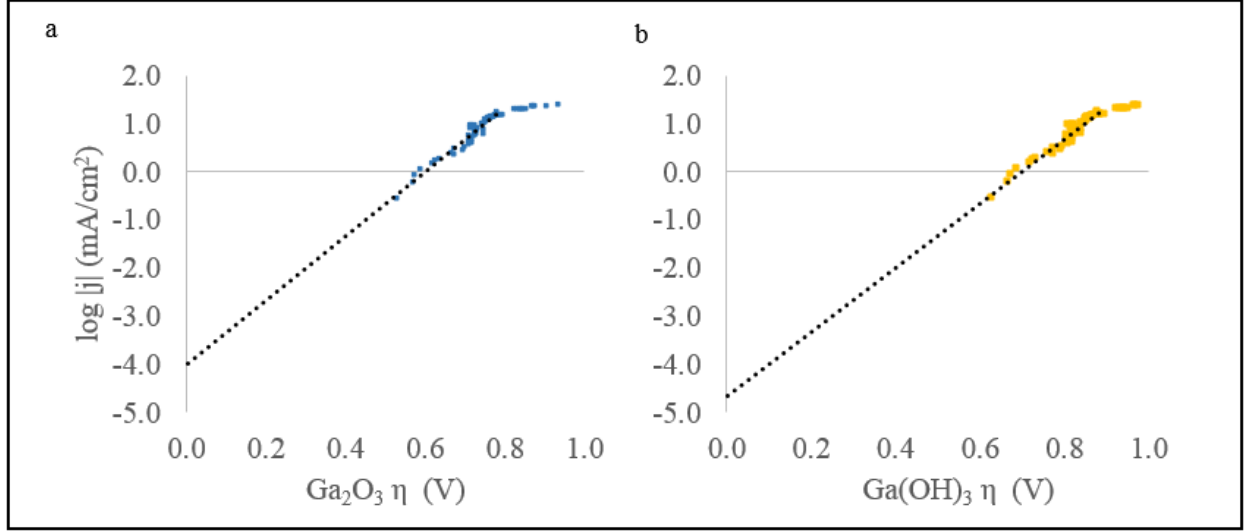


Figure 27: Tafel plots for Ga-air cell with 33.6 wt.% KOH wetted anion exchange membrane at 65°C. Overpotential shown for gallium oxide (a) and gallium hydroxide (b)

Table 7: Kinetic Modeling Parameters Determined from Tafel Plots for Gallium Oxide and Gallium Hydroxide.

Electrolyte Configuration	Anodic Oxidative Species	Tafel Slope (V dec ⁻¹)	Charge Transfer Coefficient	Exchange Current Density (mA/cm ²)	Fitted Limiting Anode Current Density (mA/cm ²)
Zirconia Cloth	Ga ₂ O ₃	7.352	0.51	3.87 x 10 ⁻⁴	8.5
	Ga(OH) ₃	7.352	0.51	7.25 x 10 ⁻⁵	8.5
Anion Exchange Membrane	Ga ₂ O ₃	6.705	0.55	9.922 x 10 ⁻⁵	17
	Ga(OH) ₃	6.705	0.55	2.119 x 10 ⁻⁵	17

4.3.3 Polarization Modeling.

An approximate model to predict polarization curves of Zn-air batteries was developed by White (2005) based on Butler-Volmer reaction kinetics coupled with diffusional limitations at each electrode for Zn-air batteries, shown in Equation 18.

$$V = V_0 - \frac{RT}{\alpha_A F} \sinh^{-1} \left[\frac{1}{2} \left\{ \frac{i_A}{i_{A,0}} / 1 - \frac{i_A}{i_{A,L}} \right\} \right] - \frac{RT}{\alpha_C F} \sinh^{-1} \left[\frac{1}{2} \left\{ \frac{i_C}{i_{C,0}} / 1 - \frac{i_C}{i_{C,L}} \right\} \right] - i \left(\frac{L_{KOH}}{\sigma_{KOH}} \right) - i R_i \quad (18)$$

This model takes into account the overpotential loss from both electrodes, the electrolyte ionic conductivity loss and the electronic conductivity loss. This equation was used with the parameters shown in Table 8 to model the Ga-air cell.

Table 8: Parameters used for gallium-air battery polarization modeling.

UNIVERSAL CONSTANTS			
Parameter	Value or Expression	Unit	Reference
F	96,485	C/mol	(Dean and Lange, 1999)
R	8.314	J/mol K	(Dean and Lange, 1999)
OPEN CIRCUIT VOLTAGE			
V_{0,Ga_2O_3}	1.717	V	Calculated
$V_{0,Ga(OH)_3}$	1.643	V	Calculated
AIR CATHODE OVERPOTENTIAL PARAMETERS			
α_C	$\alpha_O = \alpha_O^0 * T$ $\alpha_O = 0.0016878 * T$		(Song and Zhang, 2008) ¹ (Song & Zhang, 2008) ¹
$i_{C,0}$	$I_{O_2}^0 = I_{O_2}^0 e^{-Ea/RT}$ $I_{O_2}^0 = (9.89 * 10^{-6} Acm^{-2}) e^{-Ea/RT}$ $I_{O_2}^0 = (9.89 * 10^{-6} Acm^{-2}) e^{-57.3/RT}$	A/cm ²	(Song and Zhang, 2008) ¹ (Qiol et al., 2013) ² (Song & Zhang, 2008) ¹
$i_{C,L}$	$6.56 * 10^{-11}$	A/cm ²	(White, 2005)
LIQUID GALLIUM ANODE OVERPOTENTIAL PARAMETERS			
α_A	0.51 (Zirconia Cloth) 0.55 (Anion Exchange Membrane)		Fitted from Tafel Plot
$i_{AGa_2O_3,0}$	$3.87 * 10^{-4}$ (Zirconia Cloth) $9.922 * 10^{-5}$ (Anion Exchange Membrane)	A/cm ²	Fitted from Tafel Plot
$i_{AGa(OH)_3,0}$	$7.25 * 10^{-5}$ (Zirconia Cloth) $2.119 * 10^{-5}$ (Anion Exchange Membrane)	A/cm ²	Fitted from Tafel Plot
$i_{A,L}$	$i_{AL} = \left(\frac{V_{A,e^-}}{-V_{A,OH^-}} \right) F \gamma_{MA} P_{OH^-,A} C_{OH^-,B}$	A/cm ²	Fitted (White, 2005)
ELECTROLYTE OVERPOTENTIAL PARAMETERS			
σ_{KOH}	$\sigma_{KOH} = K_1(100 * w) + K_2(T) + K_3(T^2)$ $+ K_4(T * 100 * w)$ $+ K_5(T^2(100 * w)^{K_6})$ $+ K_7 \left(\frac{T}{100 * w} \right) + K_8 \left(\frac{100 * w}{t} \right)$	S/cm	(Gilliam et al., 2007) ³
L_{KOH}	0.22	cm ²	Measured
iR_I	0	V	Assumed

¹For oxygen reduction reaction on a Pt. catalyst.

²Exchange current density for oxygen reduction reaction on a Pt. catalyst with 33.6 wt.% KOH.

³KOH ionic conductivity as a function weight percent (100 * w) and temperature (T). Empirically fit correlation constants (K_n) found in Figure 28.

correlation constant	value	units
K_1	0.279 844 803	S/cm
K_2	-0.009 241 294 82	S/(cm K)
K_3	-0.000 149 660 371	S/(cm K ²)
K_4	-0.000 905 209 551	S/(cm K)
K_5	0.000 114 933 252	S/(cm K ²)
K_6	0.176 5	
K_7	0.069 664 851 8	S/(cm K)
K_8	-28.981 565 8	S K/cm
K_9	-0.003 420 006 14	S/(cm K)
K_{10}	1.196 997 71 $\times 10^{-5}$	S/(cm K ²)
K_{11}	-1.172 980 91	S L/(cm mol)
K_{12}	-0.005 167 940 41	S L/(cm mol) ²
K_{13}	0.003 282 926 38	S L/(cm K mol)
K_{14}	119.604 837	S L K/(cm mol)
K_{15}	0.000 624 311 676	S L ³ /(cm mol ³)
K_{16}	-1.883 200 99 $\times 10^{-7}$	S L ² /(cm mol ² K ²)

Figure 28: Correlation constants relating conductivity of KOH by weight percent and temperature.

The cathodic polarization parameters used in the model were primarily based on literature review of the known oxygen reduction reaction on a platinum catalyst in presence of aqueous alkaline electrolyte. Anodic polarization parameters were developed based on fitting experimental data because there is no available literature to reference. Electrolyte related polarization loss parameters were also known through literature review. The results of the polarization model with varying current densities and the respective polarization loss can be found in Figure 29.

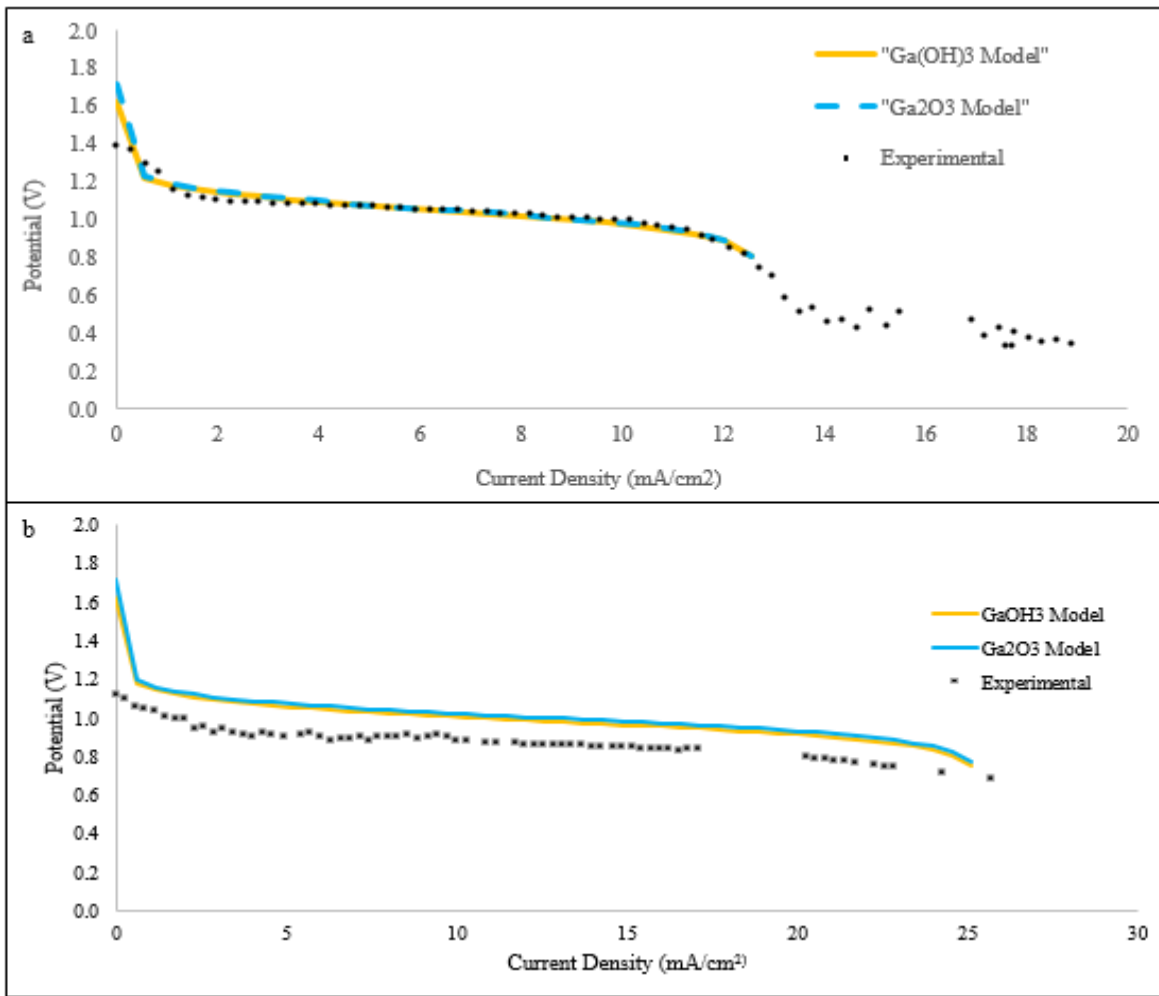


Figure 29: a) Model for Ga-air cell with zirconia cloth compared to experimental data. b) Model for Ga-air cell with an AEM compared to experimental data.

4.4 Discharge Performance: Establishing a Baseline

In order to establish a baseline performance for the gallium air cell, tests were run under the conditions listed in Table 9.

Table 9: Baseline conditions for discharge tests

Electrolyte	33.6 wt.% KOH
Separator	Zirconia Cloth
Heat Source	Heating Lamp
Current	0.5 mA
Current Density	1.41 mA/cm ²
Cell Orientation	Cathode facing down
Ambient Temperature	40 - 50°C

The electrolyte used was 33.6 wt.% KOH, chosen because it displays the highest ionic conductivity at this concentration. The heating lamp was used to ensure that the cell stayed above the melting point of gallium at a nearly constant temperature. These tests were run using a current of 0.5 mA using the BAWIN500 program from Battery Metric. The chosen current stems from the polarization curve studies of the systems.

One of the major focuses of these tests included the reproducibility. Because the cells were hand assembled each time, there was room for variability. These tests on average lasted 5 hours, with the longest test lasting just over 16 hours. Tests that lasted less than 2 hours generally experienced some form of human error such as minimal contact between the layers of the cell or overtightening. Overtightening the cell would cause the gallium to leak through and around the separator, coming into contact with the gas diffusion layer. This resulted in the cell short circuiting. Figure 30 shows the result from a cell short circuiting.



Figure 30: Image of a short circuited cell attributed to gallium leakage

In comparison, commercial zinc-air button cells can last around 80 hours as reported in the performance metrics from Duracell. Figure 31 and Figure 32 compare the Ga-air discharge to an average Zn-air discharge. The Zn-air cell can withstand larger currents than the gallium cell. This is large in part due to the good design of the Zn-air cell as well as due to the difference in exchange current density, as demonstrated previously by the Tafel plots as discussed above.

Figure 31 shows the most a 12 hour discharge of the gallium air cell under the baseline testing conditions. It was achieved at an ambient temperature of 40°C to ensure that the gallium was liquid. This test lasted 12 hours and the potential remained relatively constant throughout the entirety of the test.

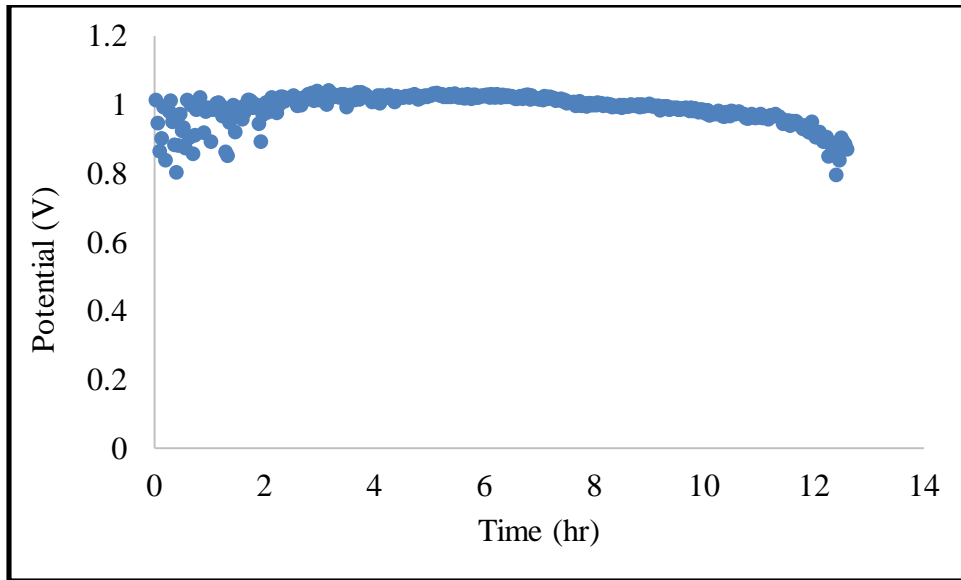


Figure 31: Ga-air cell discharge curve at 40 °C

Figure 32 shows a discharge plot obtained for a commercial Zn-air button cell (model 675) using the BAWIN500 program. This test lasted just over 80 hours with a starting OCV of approximately 1.3. The current drawn from this cell was 7 mA which is significantly higher than the 0.5 mA current used in the gallium-air tests. The discharge curve was relatively flat for the first 40 hours and remained above 1 V until about 70 hours of discharge. Clearly, there is significant room for improvement in the performance of the Ga-air cell.

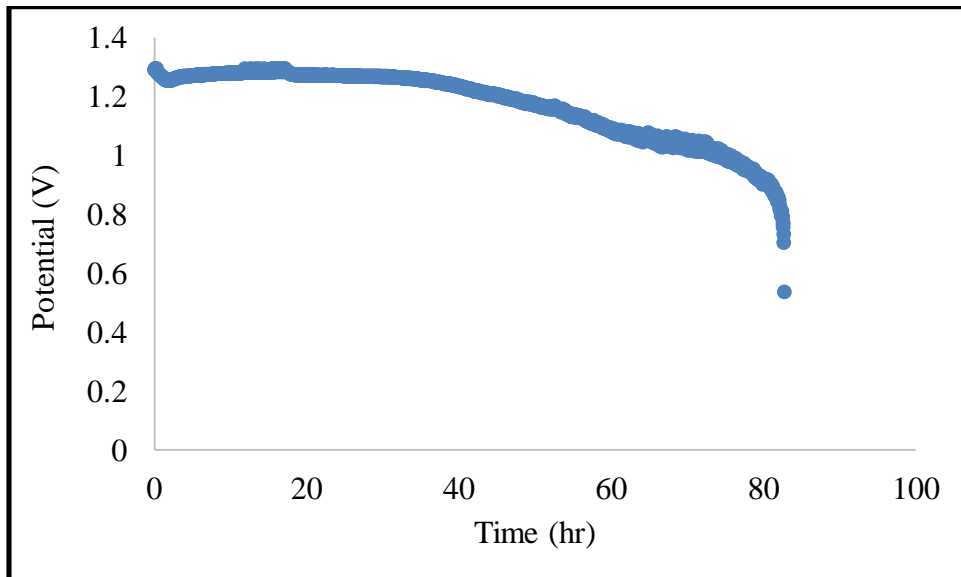


Figure 32: Zn-air button cell discharge at room temperature

Figure 33 shows the previous discharge curve plotted versus capacity. The capacity this particular cell reached was just over 6 mAh. Based on theoretical calculations and the total mass, the capacity of the cell would be 1400 mAh. Therefore, the cells constructed were immensely underperforming. However, because the entirety of the gallium is not in contact with the electrolyte, as it is in the Zn-air cell, the actual mass of the anode would be much smaller and the theoretical capacity would reflect that. Based on the volume (0.017 cm^3) of the thin oxide/hydroxide film (assuming a 0.5 mm thickness) that resulted in some tests on the separator, the capacity was calculated to be about 115 mAh. Figure 33 shows the capacity achieved by the baseline test previously in Figure 31.

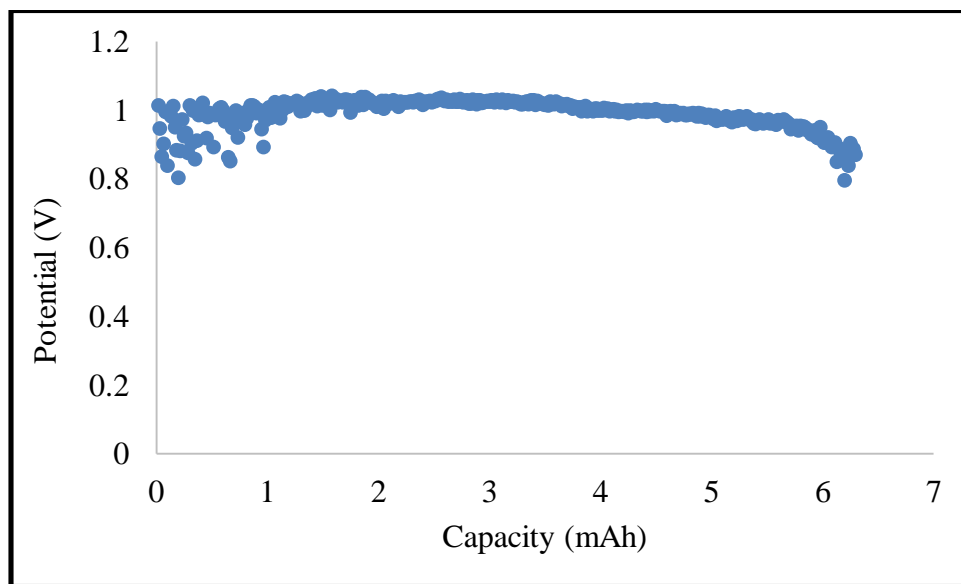


Figure 33: Ga-air cell potential vs capacity

The actual capacity of the Ga-air, thus, cell proved to be much lower than its theoretical value for the entirety of the gallium's mass and even lower than the calculated capacity from the thin oxide film formed next to the separator. Factors that impacted the capacity of the cell include the limited surface area of the anode, or mass transfer limitations. The gallium anode, is contained within a stainless steel crucible within the Swagelok cell. Between the anode and the separator was a gasket leaving only the area of space within the gasket to come into contact. If the cell were to be continuously mixed, with electrolyte or a conducting oxide, similar to a flow battery, the cell may not experience the same limitations. Further, it is likely that the electrolyte layer in

the cell dried out. The Zn-air cell has a hydrophobic GDL at the oxygen electrode which might retain moisture better in the commercial air cell.

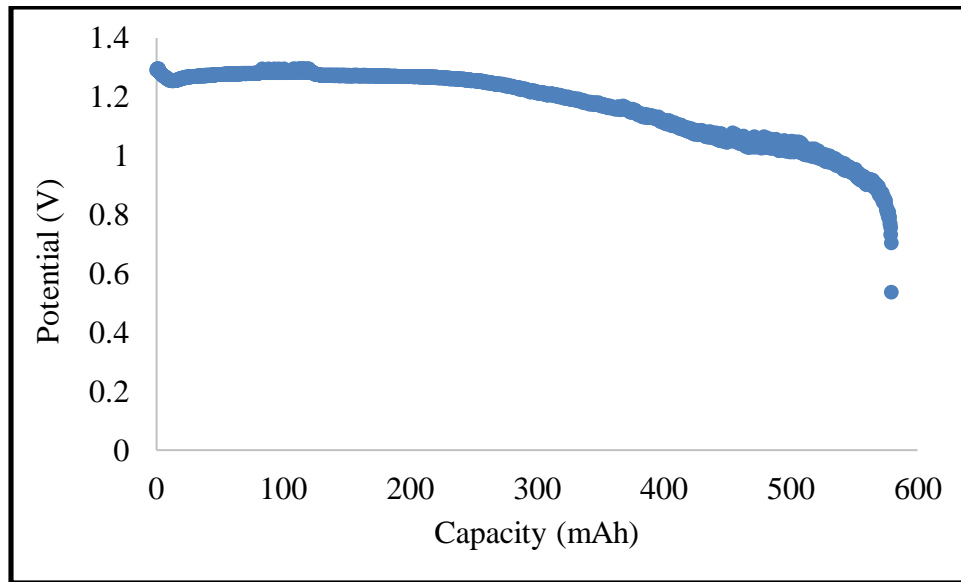


Figure 34: Zn-air cell potential vs capacity discharge curve

The commercial Zn-air cells tested have a rated capacity of around 600 mAh, and the discharge tests achieved a capacity just under 600 mAh. These cells, as previously mentioned, are able to withstand higher currents, as studied in the polarization tests, and longer discharge periods. One of the likely reasons for its high performance metrics lies within the design of the cell. Zn-air batteries use a zinc slurry suspended in an electrolyte. Because the zinc used is smaller particles, as opposed to one large slab, there is much more active metal surface area within the cell. The mixing of the zinc powder and the electrolyte alleviated some of the issues relating to mass transfer and allowed for continuous ionic conductivity throughout the electrolyte with more area for reactions to occur. Thus, Zn-air's success is related to its internal design and its consistent manufacturing process.

Based on the chemistry of the cell carbonation of the electrolyte, the separator drying out, and an oxide layer forming and blocking the cell were determined to be three factors that would inhibit the performance of the gallium air cell. These factors were tested for and their results compared

with the standard gallium air cell to determine the limiting factor of the Ga-air cell. Additionally, further tests were performed to study the effect of temperature on the battery's performance.

4.5 Discharge Performance: Effect of Variables

Throughout the course of testing, many minor adaptations were made to each test in order to increase the discharge time of the liquid gallium-air cell. Standard testing began with a zirconia cloth separator wetted with 33.6 wt.% KOH for approximately 15 minutes, under a heat lamp at approximately 60 °C, with cell inversion to ensure maximum surface contact. Discharge of the cell was performed with a 0.5 mA current with a focus to maximize the total discharge time of the cell.

Of the standard zirconia cloth separator tests, one result lasted a total of 12.6 hours at an average temperature of 39.3°C. The exact discharge curve is depicted in Figure 35.

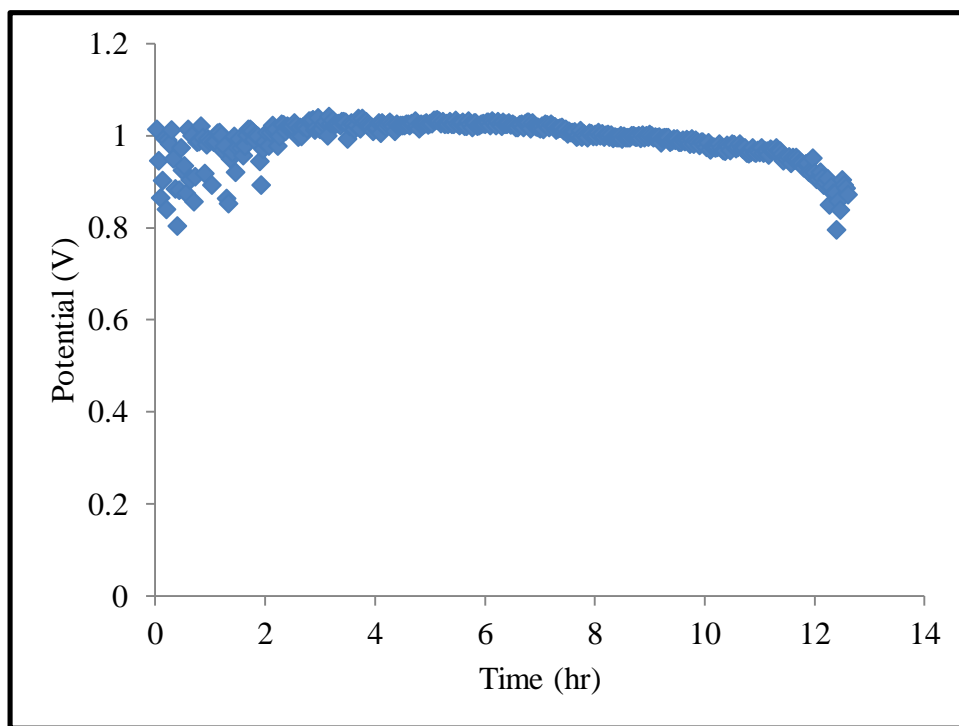


Figure 35: 12.6 hour discharge time with zirconia cloth separator

The reason for this result could be attributed to a variety of factors such as cell tightness or internal cell temperature. Nevertheless, this is much longer than the average discharge time of 4.7 hours for zirconia cloth tests. However, duplicating this result proved to be very difficult

when using zirconia cloth at low temperatures, since maintaining an internal temperature above 30°C to prevent gallium solidification was challenging without the separator drying out.

To investigate the potential issues of oxide formation on the separator, limiting cell performance and life, cell agitation was performed. The best result for cell revival after agitation is shown in Figure 36.

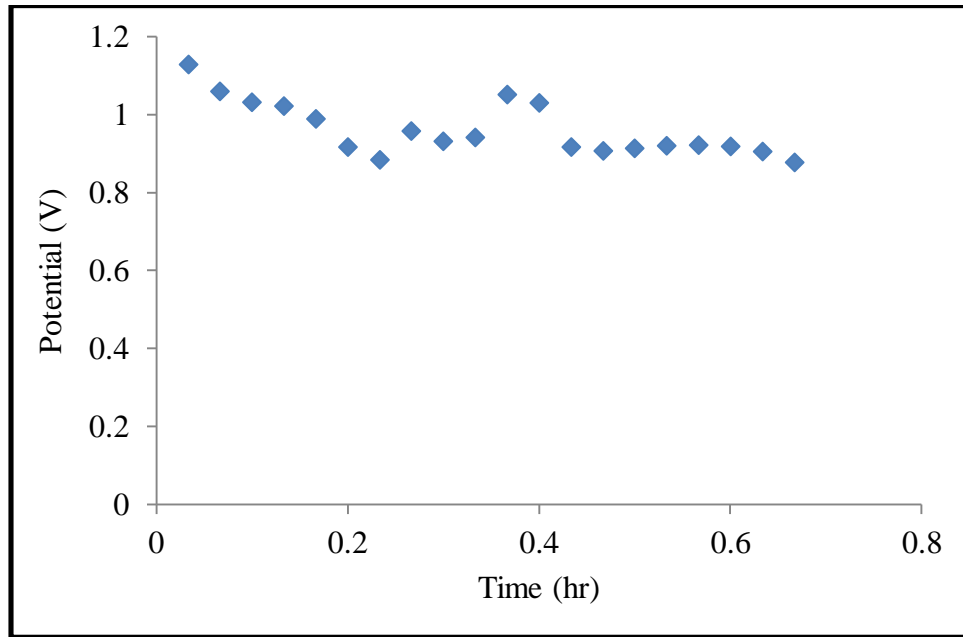


Figure 36: The effects of cell agitation on zirconia cloth discharge performance

Another method that was attempted to extend the discharge time of a zirconia cloth was the attempted use of a porous PTFE layer between the GDL and the separator, to minimize separator drying. The results of this test are pictured in Figure 37.

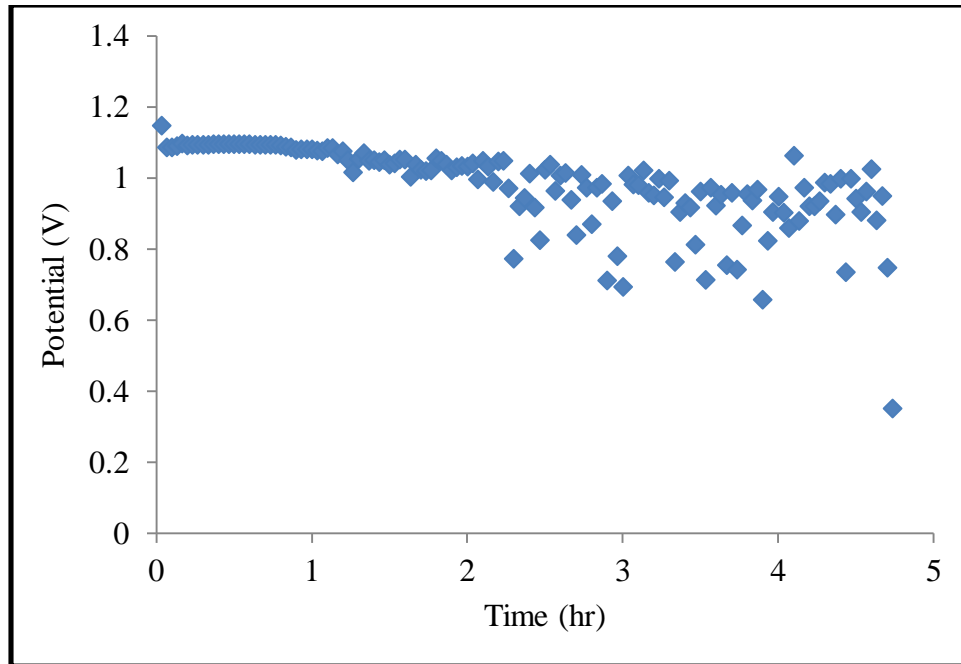


Figure 37: The addition of PTFE to zirconia cloth separator

Thus, the inclusion of PTFE achieved a total discharge time of 4.7 hours at temperature of approximately 68.9 °C. This value is comparable to the average discharge performance of zirconia cloth, demonstrating that PTFE inclusion had little effect on the overall discharge time of the cell. However, it should be mentioned that the inclusion of PTFE allowed for a comparable discharge time at a higher average temperature to tests without it at lower temperatures. Further, it is possible that the placement of the porous PTFE layer between the GDL and the separator was not optimal, and could have reduced ionic contact between the GDL and the separator. This warrants further investigation and a study of how this is done in the commercial zinc air cell.

Temperature plays a key role on the performance and discharge time of a cell. This relation was demonstrated in metal air batteries (Zhou, 2014) correlating higher temperatures to overall lower discharge times. For this investigation, a more precise relation between temperature and discharge time was studied. Tests with zirconia cloth were performed at 40 °C, 50 °C, 60 °C, and 70 °C. The average discharge performance of the cell is shown in Figure 38 at each temperature superimposed on one another.

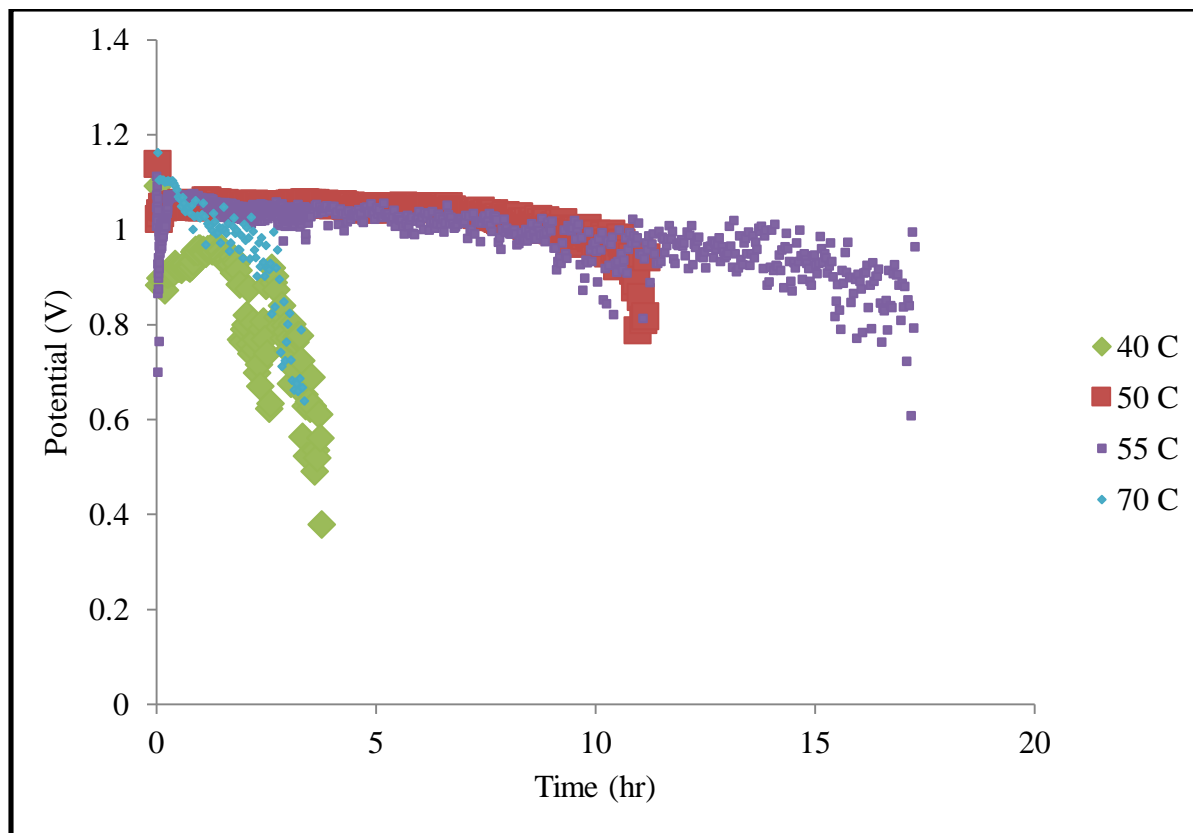


Figure 38: Each discharge test for zirconia cloth at various temperatures

From the results, it was gathered that an optimum temperature for the Ga-air cell was between 50 and 60 °C. The tests at greater temperatures lasted about a third of the time than the test at 55 °C. It is speculated that this is due to the separator drying out faster at higher temperatures. Additionally, the tests at 40 °C also only lasted around 5 hours. When these cells were disassembled, it was observed that the gallium remained solid (the temperatures measured were that of the ambient air, not within the cell). The shorter discharge time is attributed to the solid state of the cell. This is because the liquid metal is able to achieve a better contact with the separator than the solid metal.

To observe the effects of temperature at values above 70 °C, the cell had to be placed inside an oven with a temperature controller that cycled. Oftentimes, these tests would surpass 100 °C, averaging at 103.7 °C, which rapidly accelerated the drying of the cell separator. Naturally, this

had a detrimental result on the overall discharge time. These exact results are depicted in Figure 39.

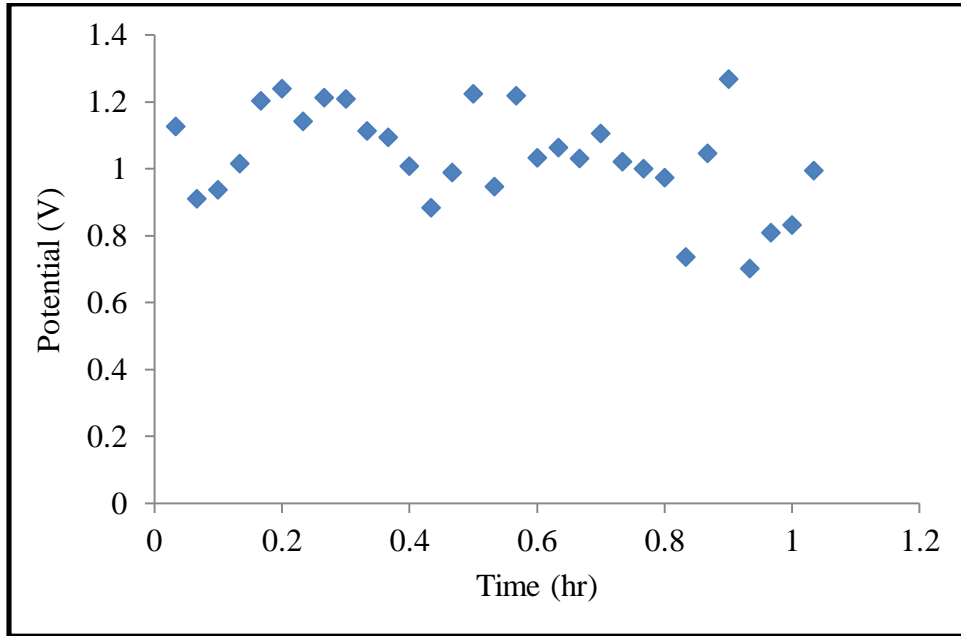


Figure 39: Discharge curve of zirconia cloth at 88°C in an oven

In Figure 39, the discharge time was only 1.0 hour. These results are significantly lower than discharge results at lower temperatures, which show due to the much more rapid drying of the separator. Moreover, the rate of carbonation would also rapidly increase with temperature. Additionally, Figure 39 contains a significant amount of oscillations in voltage throughout the discharge duration. One possible explanation for this is that the temperature in the oven oscillated significantly, which would explain why this behavior is much more common for tests with the oven.

Another method that could dry out the zirconia cloth layer more quickly would be a continuous stream of dry oxygen. For this reason, the cell was also investigated with a supply of pure O₂, and the discharge is shown in Figure 40.

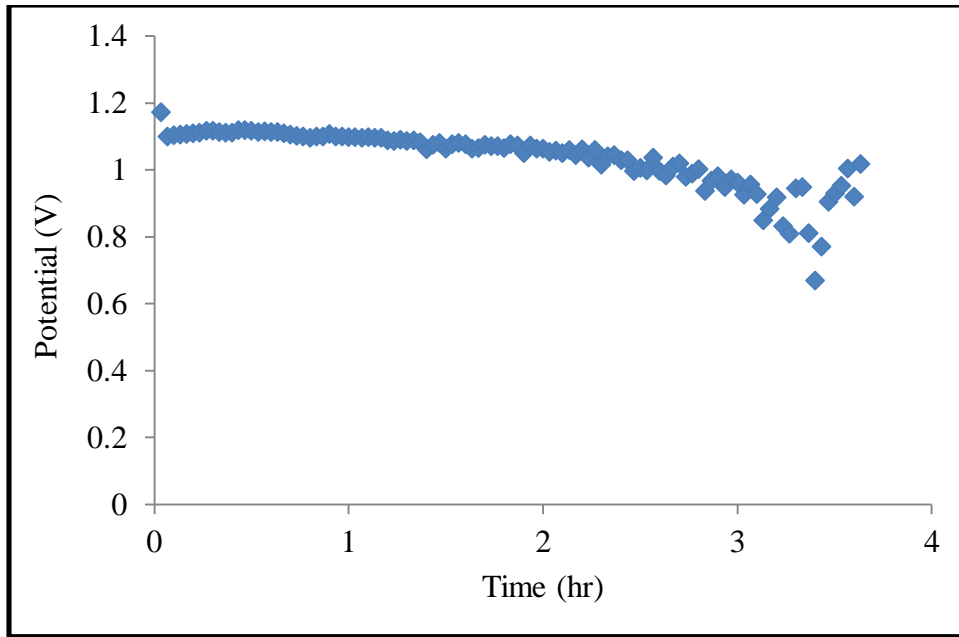


Figure 40: Discharge with zirconia cloth separator with a pure O₂ feed at approximately 40°C

This result was significantly longer than oven tests at much higher temperatures, but was also notably worse than test that were open to ambient conditions. If the performance of the cell is indeed limited by the separator drying out, then the addition of a few drops of water to the separator should revive its performance. The discharge cell shown in Figure 40 was re-wetted with 3 drops of water upon test termination, which yielded the result in Figure 41.

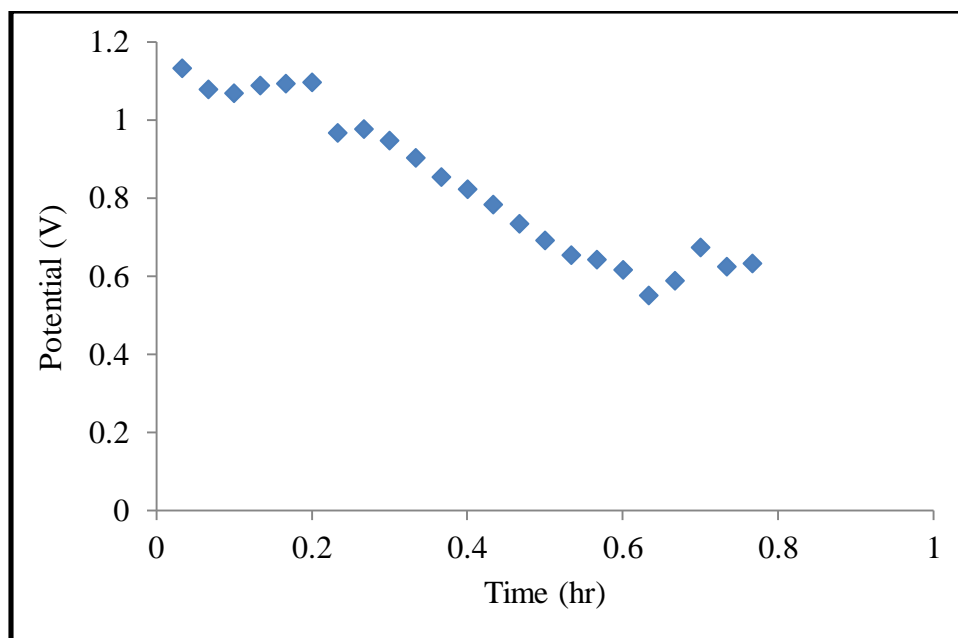


Figure 41: Discharge results of Figure 40 upon re-wetting after termination with a pure O₂ feed at approximately 40°C

This test discharged for another 0.6 hours, which is comparable to the oven discharge results. For this reason, separator drying is an important issue that must be addressed in testing, but because re-wetting did not return the cell to near-peak performance, there are other factors that also affect the discharge time.

Carbonation was postulated to be a factor that would also reduce discharge time. This process proceeds according to the following reaction:



The product of this reaction, is undissociated and therefore can precipitate onto the separator and cell. To test this, discharge cycles were performed with an anion exchange membrane (AEM) as the separator for the electrolyte layer, as opposed to zirconia cloth. AEMs have an OH⁻ ion, similar to KOH, however it is a polymer attached to a hydroxyl ion, R-OH. The R group in the AEM does not carbonate readily as the potassium in KOH does. The result was an average discharge time of 6.3 hours with a maximum of 16.1 hours. This is a significant increase in performance from the zirconia cloth performance. The longest duration AEM discharge test is in Figure 42.

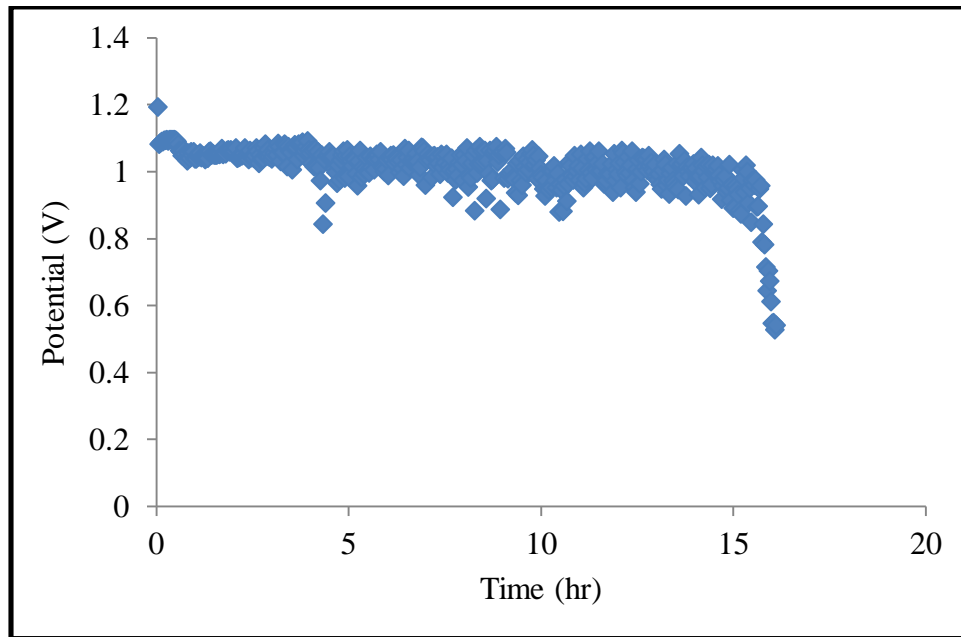
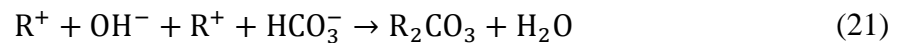
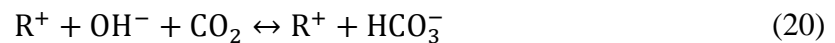


Figure 42: Discharge test results of AEM separator

Because of the dramatic increase in performance, it is clear that the separator is the key limiting factor of cell performance. The AEM had a longer discharge time than the zirconia cloth separator most likely because the composition of the AEM is more resistant to carbonation. The reaction that has to occur for the AEM to carbonate is as follows:



Because the products are still partially ionized, expect R_2CO_3 , it is still conductive in the presence of CO_2 . However, it is still susceptible to drying out, which resulted in a discharge time that is still only 0.2% of the theoretical result (~3000 hours).

5 Conclusions and Recommendations

This project developed the preliminary design of a Ga-air electrochemical cell and investigated its feasibility. This work showed that the liquid metal-air battery was feasible and identified limiting factors within the cell. The Ga-air cell was significantly outperformed by commercial Zn-air cells, however this was in part due to the highly developed design and research that has contributed to the commercialization of these batteries. The Zn-air cell, as mentioned previously, uses a three dimensional anode design with a zinc slurry mixed within the electrolyte allowing for much greater interfacial contact area than in the liquid Ga-air cell. This fact, combined with a gelled electrolyte and hydrophobic GDL, has contributed to Zn-air's success. Despite the time constraints related to this project, the cell was designed, assembled, and was able to perform for a maximum discharge time of 17 hours with a relatively constant voltage. Although not all of the initial goals were able to be reached by the end of this project, the final product was able to demonstrate reproducibility, the effect of liquid metal, and identification of several limiting factors. Addressing these limiting factors could ultimately allow for the liquid gallium-air to improve.

The primary reasoning in choosing gallium as the anode was due to its low melting point. Through many tests, it was determined that liquid gallium was able to perform better than its solid counterpart. This is due to the enhanced contact between the electrolyte and the anode due to the configuration of the cell (cathode facing down). Throughout testing the reproducibility was variable as the cells were hand assembled each time. If the cell was tightened too much, the cell would short circuit. If the cell was tightened too little, there would be limited contact between layers and the cell would underperform.

The electrolyte proved to be the source of many of the limitations of the cell. Three major factors that hindered the performance were determined through testing. These included possible carbonation of the potassium hydroxide, the drying out of the separator (considering the electrolyte was an aqueous solution), and an oxide layer forming and possibly limiting the transport of ions. The primary factor determined was the drying out of the separator. After rewetting the separator, the tests would often last another couple of hours when discharged. The oxide layer removal showed to increase the discharged cell's OCV back to just above the starting OCV, however the discharge would only last about 20 minutes. A full estimation on the potential

effect of carbonation was not able to be determined, but based on the tests using the AEM, it appears to have a strong effect as well.

In moving forward with future initiatives involving the Ga-air cell, there are several areas of testing recommended to be explored. Several avenues of interest were unable to be properly researched due to the time constraints related to this project. It is recommended that further testing focuses on the electrolyte of the battery as well as its capability of successfully recharging. It is also recommended that the use of different discharge currents is explored to see if the battery would be able to handle a greater load. Although these aspects were briefly touched upon, there is a vast area to explore especially in relation to the improvement of the battery. One possible way to enhance the discharge time may be to emulate the Zn-air cell; for instance, use a gelled mass of liquid gallium and KOH electrolyte in the anode chamber.

Although charging was not the top priority of this project, it is a key aspect regarding the intention of the battery. It is recommended that an in depth study of the charging capabilities of the battery be completed. If the liquid metal-air battery is able to be recharged it will have a significant advantage over commercialized primary metal air batteries. Additionally, such a success could lead to investigations involving other low melting point metals, alloys, and eutectics. Showing that the battery can be successfully cycled between charging and discharging will prove its potential as a microgrid energy storage device.

The electrolyte, as previously described, was found to be the key source of limitation for the cell performance. Future tests should involve changing the electrolyte to optimize the performance of the battery and eliminate or lessen factors such as drying out or carbonation. Possibilities that have been reviewed but not pursued include ionic liquids and molten salts. Additionally, it is recommended that further research is performed involving the anion exchange membranes to determine if it is the thickness of the AEM that allows for a greater life or if it is due to the properties of the AEM preventing carbonation.

Finally, the design of the battery should be developed further. In order for this battery to develop faster, different design options should be explored. Included is a flow battery style design. This battery's inspiration has roots in flow battery technology. It is possible that a flow battery style design could prove to be advantageous involving the charging capabilities of the battery.

Additionally, designing a battery made up of smaller cells creating a stack could work to increase the power of the battery.

Further research may work to bring the battery up to microgrid storage level. To reach this point, the areas mentioned should be explored as well as other limiting factors that may be discovered. The Ga-air cell, if and once proven to be rechargeable, has the potential to be used to help integrate intermittent renewable energy sources into small communities and microgrids. The oxygen electrode will also need to be developed further, since the use of platinum catalyst will be too expensive to be used for practical applications. Instead, cheaper catalysts will need to be investigated. The key components, aside from rechargeability, will involve optimizing the design of the battery and utilizing an electrolyte that will not significantly limit the cell's performance.

References

- Abraham, K. M., & Jiang, Z. (1996). A polymer electrolyte-based rechargeable lithium/oxygen battery. *Journal of The Electrochemical Society*, *143*(1), 1-5.
- Amendola, S., Binder, M., Black, P. J., Sharp-Goldman, S., Johnson, L., Kunz, M., ... & Johnson, R. (2010). U.S. Patent Application 12/841,115.
- Armstrong, R. D., Race, W. P., & Thirsk, H. R. (1971). The anodic behaviour of gallium in alkaline solution. *Journal of Electroanalytical Chemistry and Interfacial Electrochemistry*, *31*(2), 405-411.
- Arnold, C. (2007). Batteries and Energy Storage [PowerPoint slides] Retrieved from https://www.princeton.edu/ssp/workshop/batteries/battery_workshop.pdf
- Arora, P., & Zhang, Z. (2004). Battery separators. *Chemical reviews*, *104*(10), 4419-4462.
- Berecibar, M., & Zhou, M. (2013). Estimating storage requirements for wind power plants. In Networking, Sensing and Control (ICNSC), 2013 10th IEEE International Conference on (pp. 919-924). IEEE.
- Boeing 787 aircraft grounded after battery problem in Japan. (2014). *BBC News*. Retrieved from <http://www.bbc.com/news/business-25737515>
- Bouhafs, F., Mackay, M., & Merabti, M. (2014). Communication Challenges and Solutions in the Smart Grid. Springer.
- Bradwell, D. D. J. (2011). *Liquid metal batteries: ambipolar electrolysis and alkaline earth electroalloying cells* (Doctoral dissertation, Massachusetts Institute of Technology).

- Bradwell, D. J., Kim, H., Sirk, A. H., & Sadoway, D. R. (2012). Magnesium–Antimony Liquid Metal Battery for Stationary Energy Storage. *Journal of the American Chemical Society*, *134*(4), 1895-1897.
- Businesswire, 'Eos Energy Storage Introduces Aurora Battery System At \$160/Kwh | Business Wire'. N.p., 2015. Web. 27 Apr. 2015.
- Castillo, A., & Gayme, D.F. (2014). Grid-scale Energy Storage Applications in Renewable Energy Integration: A Survey. *Energy Conversion and Management*, *87*, 885-894.
- Chan, K. Y., & Savinell, R. F. (1991). Modeling Calculations of an Aluminum-Air Cell. *Journal of The Electrochemical Society*, *138*(7), 1976-1984.
- Cheng, F., Liang, J., Tao, Z. and Chen, J. (2011), Functional Materials for Rechargeable Batteries. *Adv. Mater.*, *23*: 1695–1715. doi: 10.1002/adma.201003587
- Cheng, F., & Chen, J. (2012). Metal–air batteries: from oxygen reduction electrochemistry to cathode catalysts. *Chemical Society Reviews*, *41*(6), 2172-2192.
- Chung, Yonghwa. "Electrochemistry of Gallium". *Journal of electrochemical science and technology (2093-8551)*, *4*(1), p.1 (2013).
- Dean, J. A. and N. A. Lange (1999). *Lange's Handbook of Chemistry*, McGraw-Hill.
- Débart, A., Bao, J., Armstrong, G., & Bruce, P. G. (2007). An O₂ cathode for rechargeable lithium batteries: The effect of a catalyst. *Journal of Power Sources*, *174*(2), 1177-1182.
- Deiss, E., Holzer, F., & Haas, O. (2002). Modeling of an electrically rechargeable alkaline Zn air battery. *Electrochimica acta*, *47*(25), 3995-4010.

- Dickey, M. D. (2014). Emerging Applications of Liquid Metals Featuring Surface Oxides. *ACS applied materials & interfaces*, 6(21), 18369-18379.
- Doche, M. L., Rameau, J. J., Durand, R., & Novel-Cattin, F. (1999). Electrochemical behavior of aluminium in concentrated NaOH solutions. *Corrosion science*, 41(4), 805-826.
- Dunn, B., Kamath, H., & Tarascon, J. M. (2011). Electrical energy storage for the grid: a battery of choices. *Science*, 334(6058), 928-935.
- Egan, D. R., Ponce de León, C., Wood, R. J. K., Jones, R. L., Stokes, K. R., & Walsh, F. C. (2013). Developments in electrode materials and electrolytes for aluminium–air batteries. *Journal of Power Sources*, 236, 293-310.
- Fu, Q., Hamidi, A., Nasiri, A., Bhavaraju, V., Krstic, S., & Theisen, P. (2013). The Role of Energy Storage in a Microgrid Concept: Examining the opportunities and promise of microgrids. *Electrification Magazine, IEEE*, 1(2), 21-29.
- Fukunaga, A., Nohira, T., Kozawa, Y., Hagiwara, R., Sakai, S., Nitta, K., & Inazawa, S. (2012). Intermediate-temperature ionic liquid NaFSA-KFSA and its application to sodium secondary batteries. *Journal of Power Sources*, 209, 52-56.
- Gallium*; MSDS No. 7440-55-3 [Online]; ROTOMETALS, Inc.; San Leandro, CA; Jan, 2010, https://www.rotometals.com/v/vspfiles/downloadables/MSDS_GALLIUM.pdf (accessed April 26, 2015).
- Gilliam, R. J., Graydon, J. W., Kirk, D. W., & Thorpe, S. J. (2007). A review of specific conductivities of potassium hydroxide solutions for various concentrations and temperatures. *International Journal of Hydrogen Energy*, 32(3), 359-364.
- Goodenough, J. B., & Kim, Y. (2011). Challenges for rechargeable batteries. *Journal of Power Sources*, 196(16), 6688-6694.

- Horiba, T. (2014). Lithium-Ion Battery Systems. *Proceedings of the IEEE*, 102(6), 939-950.
- Arora, P., & Zhang, Z. (2004). Battery separators. *Chemical reviews*, 104(10), 4419-4462.
- IAE. (2014). World Energy Outlook 2014, Executive Summary. International Energy Agency, OECD/IEA, Paris. Retrieved from:
<http://www.iea.org/Textbase/npsum/WEO2014SUM.pdf>
- IAE. (2014). Renewable Energy Midterm Market Report. International Energy Agency, OECD/IEA, Paris. Retrieved from:
<http://www.iea.org/Textbase/npsum/MTrenew2014sum.pdf>
- Jayakumar, A., Vohs, J. M., & Gorte, R. J. (2010). Molten-metal electrodes for solid oxide fuel cells. *Industrial & Engineering Chemistry Research*, 49(21), 10237-10241.
- Jensen, C. (2013). Tesla Says Car Fire Started in Battery. *The New York Times*. Retrieved from
<http://wheels.blogs.nytimes.com/2013/10/02/highway-fire-of-tesla-model-s-included-its-lithium-battery/>
- Kelly, R. (2006). Apple recalls 1.8 million laptop batteries. *CNN Money*. Retrieved from
http://money.cnn.com/2006/08/24/technology/apple_recall/index.htm
- Kiehne, H. A. (2003). *Battery technology handbook* (Vol. 60). CRC Press.
- Kim, H., Boysen, D. A., Newhouse, J. M., Spatocco, B. L., Chung, B., Burke, P. J., ... & Egan, D. R., Ponce de León, C., Wood, R. J. K., Jones, R. L., Stokes, K. R., & Walsh, F. C. (2013). Developments in electrode materials and electrolytes for aluminium-air batteries. *Journal of Power Sources*, 236, 293-310.

- Kozin, L. F., & Gaidin, A. V. (2009). Kinetics and mechanism of gallium discharge and ionization in an alkaline solution of potassium fluoride. *Russian Journal of Applied Chemistry*, 82(3), 406-415.
- Lee, J. S., Tai Kim, S., Cao, R., Choi, N. S., Liu, M., Lee, K. T., & Cho, J. (2011). Metal–air batteries with high energy density: Li–air versus Zn–air. *Advanced Energy Materials*, 1(1), 34-50.
- Licht, S., Cui, B., Stuart, J., Wang, B., & Lau, J. (2013). Molten air—a new, highest energy class of rechargeable batteries. *Energy & Environmental Science*, 6(12), 3646-3657.
- Otaegui, L., Rodriguez-Martinez, L. M., Wang, L., Laresgoiti, A., Tsukamoto, H., Han, M. H., ... & Rojo, T. (2014). Performance and stability of a liquid anode high-temperature metal air battery. *Journal of Power Sources*, 247, 749-755.
- Pei, P., Ma, Z., Wang, K., Wang, X., Song, M., & Xu, H. (2014). High performance zinc air fuel cell stack. *Journal of Power Sources*, 249, 13-20.
- Rahman, M. A., Wang, X., & Wen, C. (2013). High Energy Density Metal-Air Batteries: A Review. *Journal of The Electrochemical Society*, 160(10), A1759-A1771.
- Regan, M. J., Tostmann, H., Pershan, P. S., Magnussen, O. M., DiMasi, E., Ocko, B. M., & Deutsch, M. (1997). X-ray study of the oxidation of liquid-gallium surfaces. *Physical Review B*, 55(16), 10786.
- Sadoway, D. R. (2012). Liquid Metal Batteries: Past, Present, and Future. *Chemical reviews*, 113(3), 2075-2099.

- Sarasua, A.E., Molina, M.G., and Mercado, P.E. (2013). Dynamic Modelling of Advanced Battery Energy Storage System for Grid-Tied AC Microgrid Applications, Energy Storage Technologies and Applications, Dr. Ahmed Zobaa (Ed.), ISBN: 978-953-51 0951-8, InTech, DOI: 10.5772/52219. Retrieved from:
<http://www.intechopen.com/books/energystorage-technologies-and-applications/dynamic-modelling-of-advanced-battery-energystorage-system-for-grid-tied-ac-microgrid-applications>
- Schweitzer, G. K., & Pesterfield, L. L. (2009). *The Aqueous Chemistry of the Elements*. Oxford University Press.
- Skyllas-Kazacos, M., Chakrabarti, M. H., Hajimolana, S. A., Mjalli, F. S., & Saleem, M. (2011). Progress in flow battery research and development. *Journal of the Electrochemical Society*, 158(8), R55-R79.
- Song, C., & Zhang, J. (2008). Electrocatalytic oxygen reduction reaction. In PEM fuel cell electrocatalysts and catalyst layers (pp. 89-134). Springer London.
- T. I. Popova, I. A. Bagotskaya, and E. D. Moorhead, "Gallium", A.J. Bard (ed.) *Encyclopedia of electrochemistry of the elements*, vol. 8. Marcel Dekker Inc, New York, pp 207-262 (1978).
- Varadharaj, A., & Rao, G. P. (1990, April). Cyclic voltammetric studies on gallium film electrodes in alkaline media. In *Proceedings of the Indian Academy of Sciences-Chemical Sciences* (Vol. 102, No. 2, pp. 177-187). Springer India
- Vega, J. A., Chartier, C., & Mustain, W. E. (2010). Effect of hydroxide and carbonate alkaline = media on anion exchange membranes. *Journal of Power Sources*, 195(21), 7176-7180.
- White, L. J. (2005). An approximate analytical model for the discharge performance of a primary zinc/air cell (Doctoral dissertation, WORCESTER POLYTECHNIC INSTITUTE).

Xu, M., Ivey, D. G., Xie, Z., & Qu, W. (2015). Rechargeable Zn-air batteries: Progress in electrolyte development and cell configuration advancement. *Journal of Power Sources*, 283, 358-371.

Zhou, Ruolin. (2014). The Development of Zinc Air Battery's Efficiency and Rechargeability in Molten Alkaline Electrolyte. (Masters Research Report). Worcester Polytechnic Institute, Worcester, MA.

APPENDIX

Appendix A: Anode Procedure and General Cell Assembly

The anode was prepared with liquid gallium active material and a stainless steel current collector (in the form of a crucible) according to the following procedure:

1. Liquid Gallium Preparation:
 - 1.1. Measured weight of the bottom half of the cell with the crucible (pictured).
 - 1.2. Added approximately 1.2 g of Gallium metal to the steel crucible to fill it.
 - 1.3. Applied heat from heating lamp to Gallium such that it becomes liquid.
 - 1.4. Measured weight of crucible with liquid Gallium to determine amount of Gallium used.
 - 1.5. Adjusted amount of Gallium until measured weight was 1.25g.
2. Cell Assembly:
 - 2.1. Fit stainless steel tube, Node B, into the bottom hexagonal PTFE Swagelok nut.
 - 2.2. Placed compression spring into Node B.
 - 2.3. Hand tightened middle hexagonal PTFE Swagelok union to bottom nut containing Node B.
 - 2.4. Place crucible in bottom half, measure out gallium.
 - 2.5. Assemble the layers on top of the cell:
 - 2.5.1. Gasket
 - 2.5.1.1. Teflon with an inner diameter of 6.6mm and an outer diameter of 11.8mm.
 - 2.5.2. Separator/electrolyte
 - 2.5.3. Gas Diffusion Layer
 - 2.6. Place the second node on top and screw on, hand tightening, the PTFE Swagelok nut.

Appendix B: Electrolyte Procedure

B.1 Zirconia Paper

The electrolyte layer was assembled with Zirconia separator material (ZYK-15 from Zircar, Zirconia Inc.) wetted with aqueous 33.6 wt.% KOH by the following procedure:

1. KOH Solution Preparation:
 - 1.1. Measured 3.36g of KOH (Sigma Aldrich, solid pellets $\geq 85\%$)
 - 1.2. Measured 10 mL of distilled water.
 - 1.3. Transferred KOH and water to 50 mL beaker.
 - 1.4. Mixed until KOH was dissolved completely.
2. Zirconia Separator Preparation:
 - 2.1. Cut zirconia paper using punch with a diameter of 11.8mm.
 - 2.2. Transferred zirconia separator to 6M KOH solution with forceps.
 - 2.3. Allowed separator to soak for 15-20 minutes.
3. Cell Assembly
 - 3.1. Applied gasket then separator to the exposed surface of the liquid Gallium anode material with forceps.
 - 3.2. Then add on GDL and complete the cell assembly as previously described.

B.2 Anion Exchange Membrane

For some tests, an anion exchange membrane (manufactured by Membrane International) was used to block cation permeation from the anode to the cathode; thus, preventing carbonation. The procedure used was:

1. KOH Preparation
 - 1.1. A 33.6 wt.% solution of KOH was prepared similarly to the solution used for the zirconia paper.
2. AEM Preparation
 - 2.1. Cut AEM using punch with a diameter of 11.8mm.
 - 2.2. Transferred AEM to the KOH solution using forceps.
 - 2.3. Allowed for the AEM to soak for at least 24 hours.
3. Cell Assembly
 - 3.1. Applied gasket, separator, and GDL in that order, to the exposed surface of the liquid Gallium anode material with forceps.

Appendix C: Cathode Procedure

The air cathode consisted of a carbon GDL pre-coated with platinum catalyst (LT140EW Low Temperature manufactured by E-TEK) prepared by the following procedure:

1. Air Cathode Preparation:
 - 1.1. Cut catalyzed GDL using a punch with a diameter of 11.8mm.
2. Cell Assembly:
 - 2.1. Placed catalyzed GDL at the center surface of the electrolyte separator material.
 - 2.2. Fit stainless steel tube, Node A, into top hexagonal PTFE Swagelok nut.
 - 2.3. Hand tightened the top nut containing Node A into the middle hexagonal PTFE Swagelok Union.

Appendix D: Swagelok Assembly Procedure

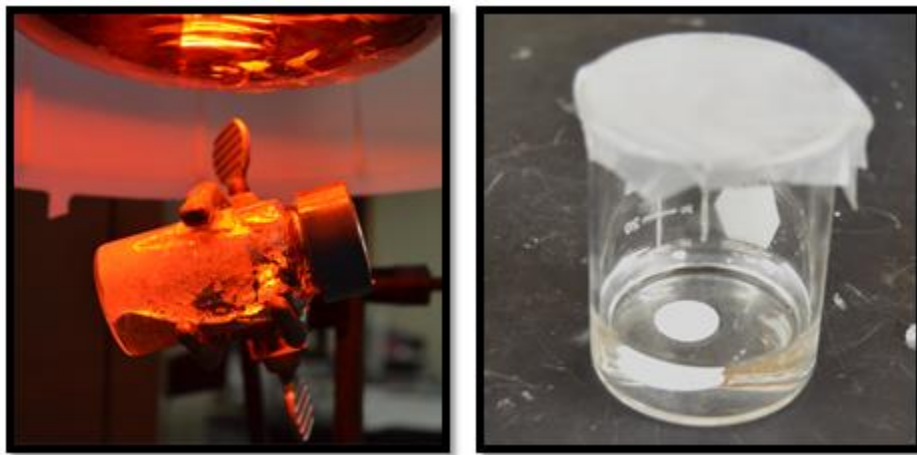


Figure 43: Heating gallium in glass vial under a heating lamp (left). Soaking zirconia cloth separator in 30 wt.% KOH (right).



Figure 44: Ferrule orientation on anode current collector (left) in Swagelok PTFE fitting (right).

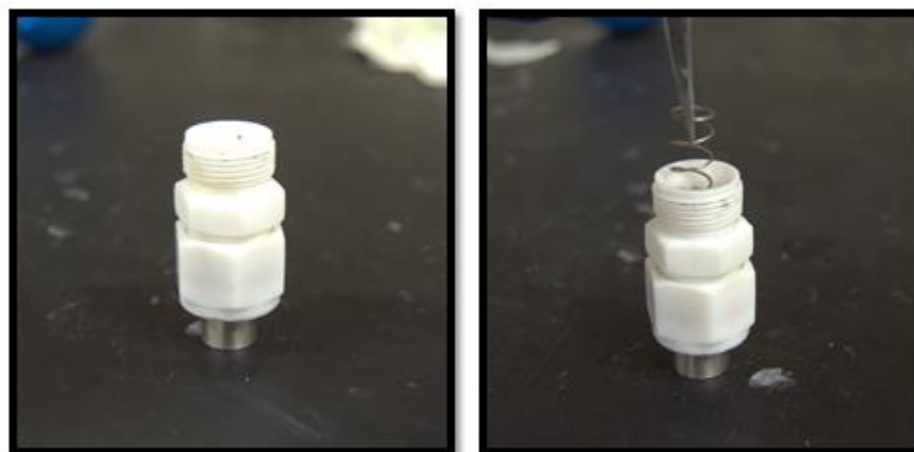


Figure 45: Swagelok PTFE union connected to fitting holding anode current collector (left). Addition of compression spring (right).



Figure 46: Addition of stainless steel crucible to top of compression spring (left). Addition of liquid gallium to the crucible using a syringe (right).

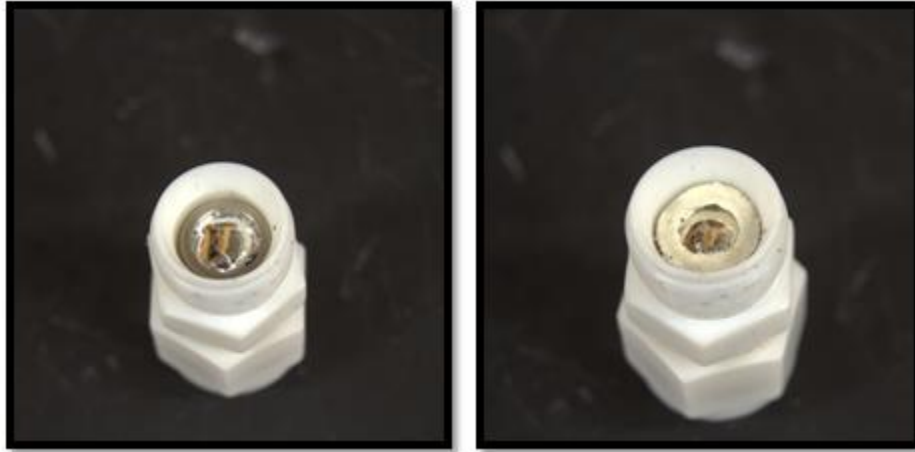


Figure 47: View of liquid gallium in crucible (left). Teflon gasket above anode crucible (right).

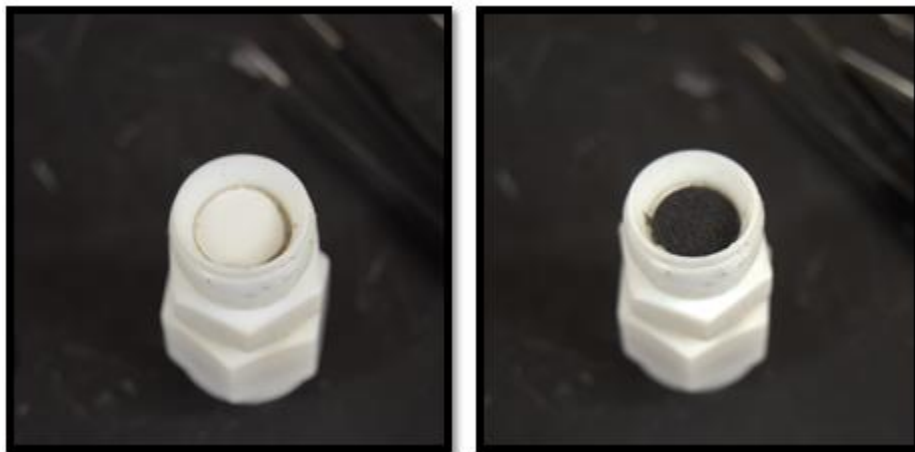


Figure 48: Zirconia cloth separator wetted with 30 wt.% KOH above the gasket (left). Catalyzed gas diffusion layer above separator, with platinum coated catalyst facing the electrolyte (right).



Figure 49: Ferrule orientation on air cathode current collector (left) with Swagelok fitting added (right).

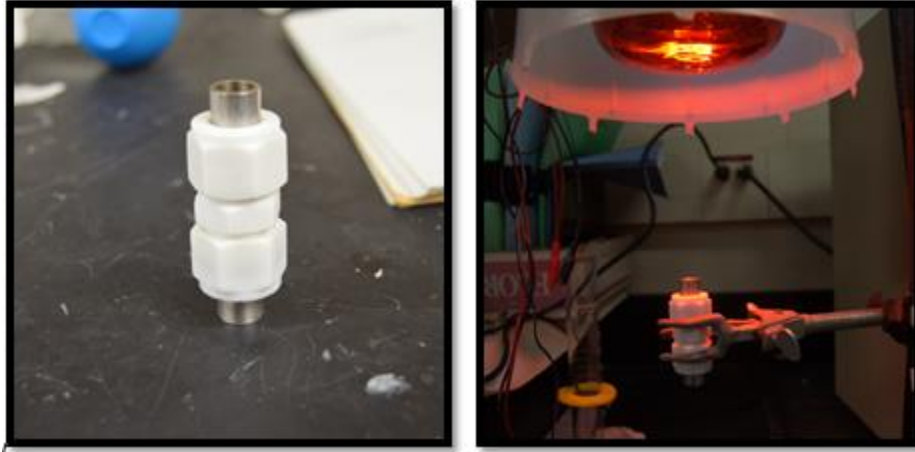


Figure 50: Completed cell configuration (left. Cell held by a ring stand clamp under a heating lamp oriented so that liquid metal anode is above the air cathode (right).

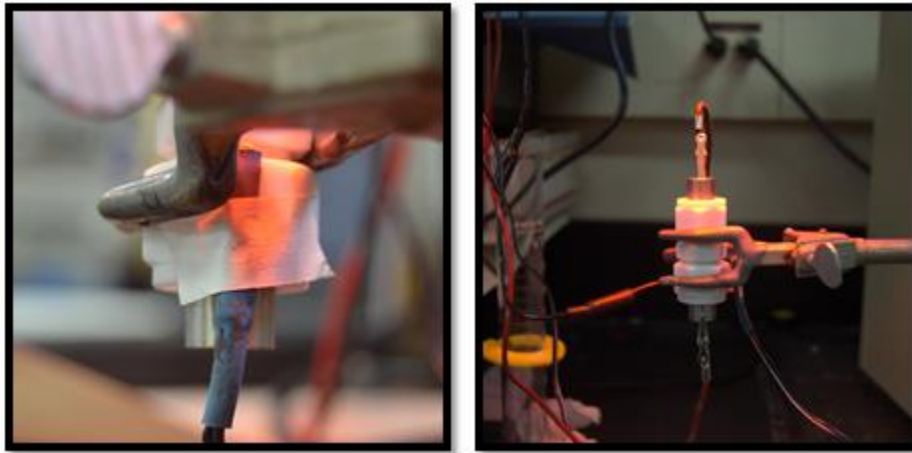


Figure 51: Taped temperature probe from battery analyzer taped to the Swagelok fitting on the air cathode side of the cell (left). Analyzer cathode and anode electrical leads attached to current collector (right).

Appendix E: Battery Analyzer Program (BA500WIN) User Guide

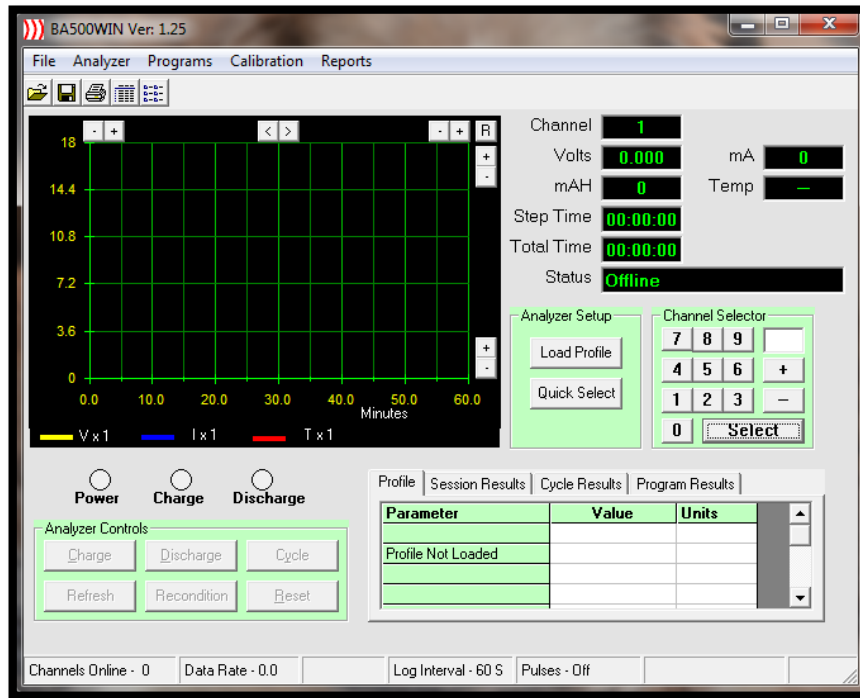


Figure 52: Start page of the BA500WIN program. Features a real time graph that charts voltage, current and temperature.

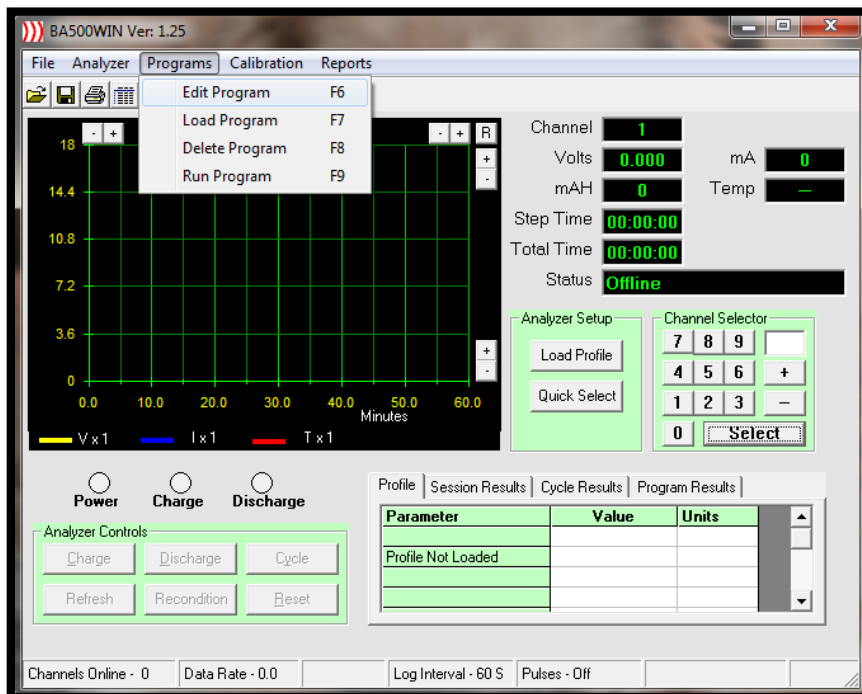


Figure 53: Programs drop down menu opened. Tests can be made with the program editor. Once saved, these programs can be run by first loading them, then clicking run program.

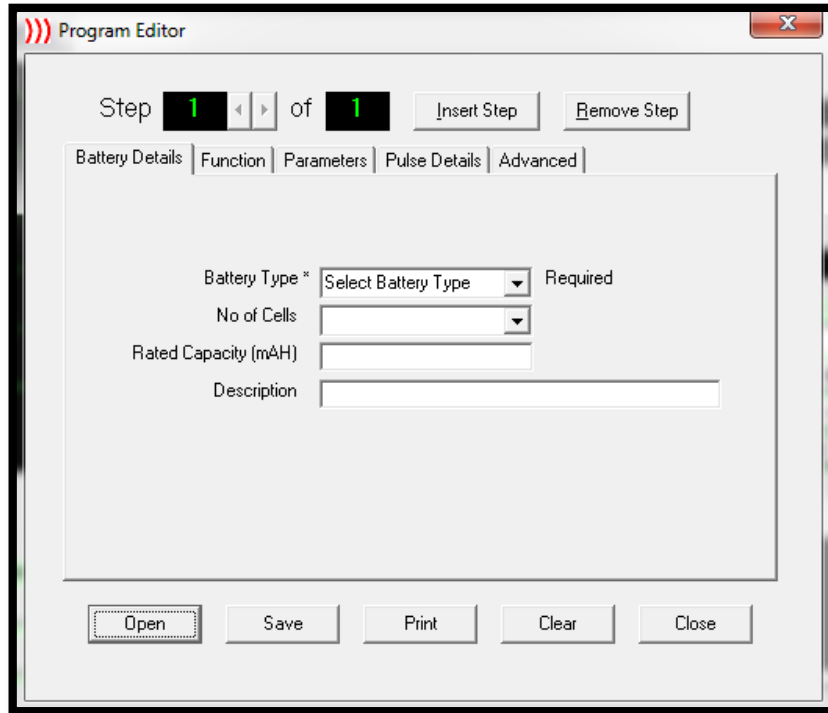


Figure 54: By choosing edit program from the programs dropdown menu, the program editor window opens.

Under the battery details tab there are several options such as battery type, number of cells, rated capacity and description. The only required field is battery type. For discharging purposes a primary non-rechargeable battery type was chosen. For instances to test charging, any of the other battery types may be chosen.

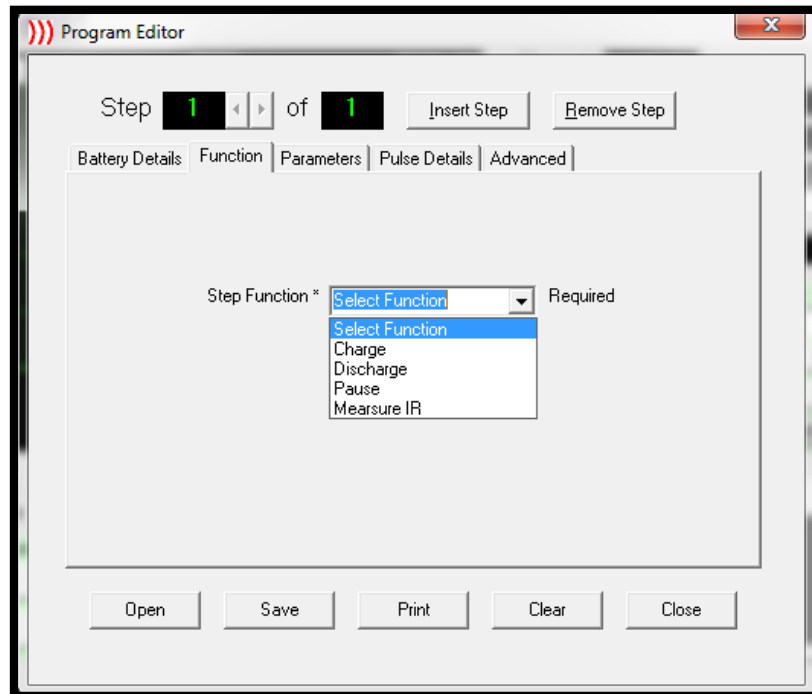


Figure 55: The second tab of the program editor requires a step function. To gather an open circuit voltage measurement, the pause function can be chosen.

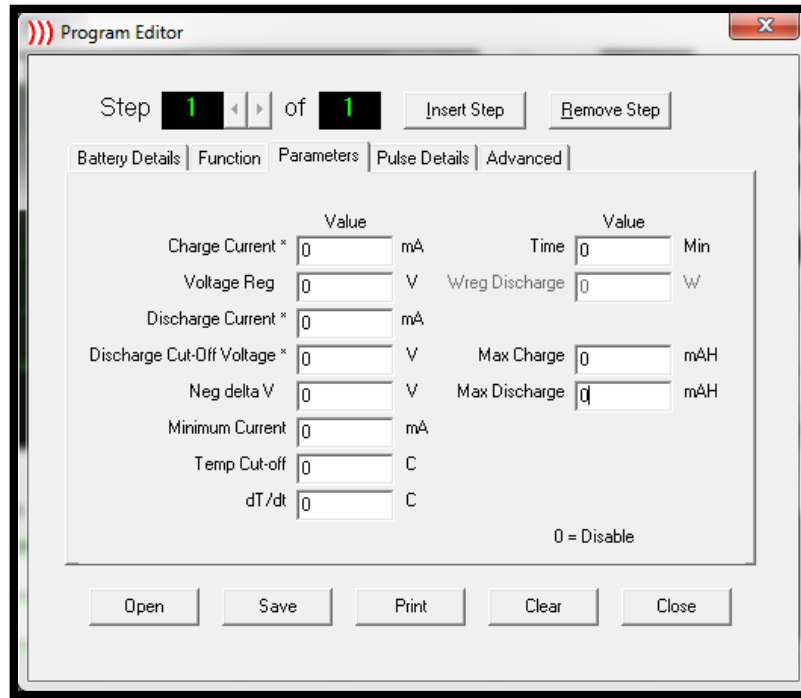


Figure 56: The third tab of the program editor lets the user define the parameters of the test.

Depending on the step function chosen before, certain parameters are required. For example, discharge tests can be conducted with a discharge current of 0.5mA to a cut-off voltage of 0.01 V while other parameters can be ignored. The other two program editor tabs, 'pulse details' and 'advanced,' can also be ignored for typical discharge tests. Additional steps with various functions and parameters can be added by the insert step button, typically an open circuit voltage measurement for a period of time followed by discharge was performed. Once completed, the file is saved in a .pg4 format and loaded from the programs menu dropdown. Once the program is run, a prompt window to save the file in a .csv format is generated for further analysis in Microsoft Excel.

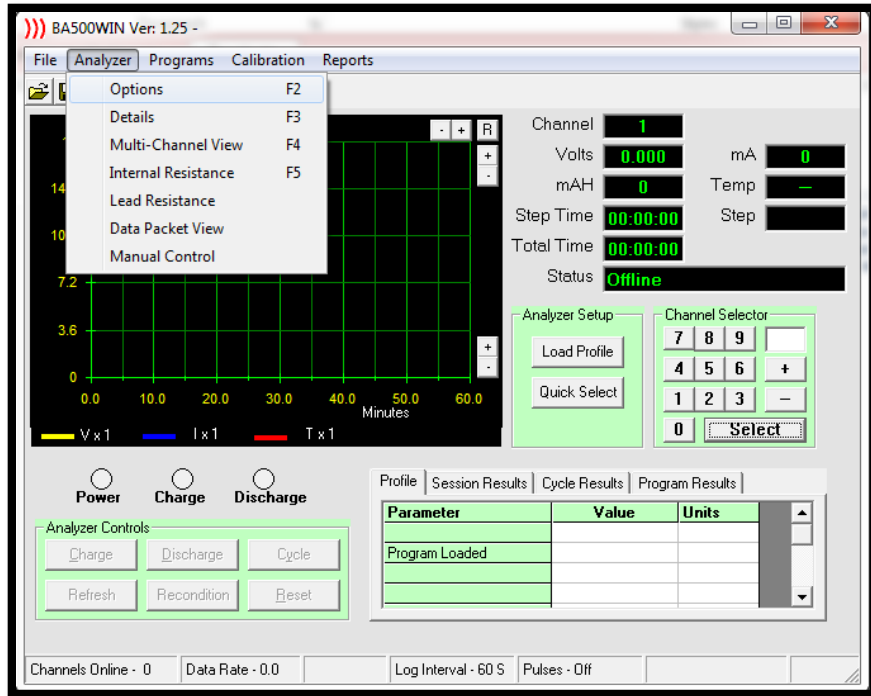


Figure 57: Often it is necessary to change the analyzer options which can be found from the drop down menu shown above or by keyboard shortcut F2.

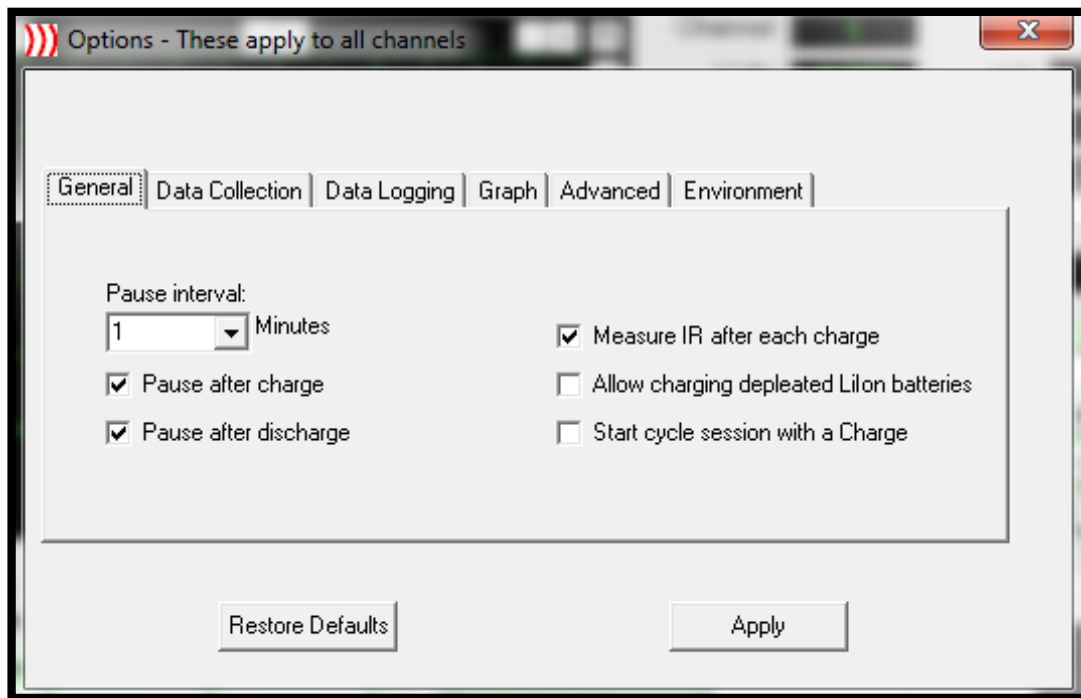


Figure 58: The analyzer options window opens when prompted to show various tabs ranging from 'general' to 'environment.' These options can be set to the user preference. For polarization curves, it is often necessary to change the data logging tab to a shorter time interval.